Available online at www.sciencedirect.com
ScienceDirect
Comput. Methods Appl. Mech. Engrg. 196 (2007) 1827–1846
Computer methods in applied mechanics and engineering
www.elsevier.com/locate/cma

Second-order accurate integration algorithms for von-Mises plasticity with a nonlinear kinematic hardening mechanism

E. Artioli [b,c,*], F. Auricchio [b,c], L. Beirão da Veiga [a]

[a] *Dipartimento di Matematica, Università di Milano, Italy*
[b] *Dipartimento di Meccanica Strutturale, Università di Pavia, Italy*
[c] *IMATI-CNR, Pavia, Via Ferrata 1, I-27100, Italy*

Received 30 May 2006; received in revised form 10 October 2006; accepted 16 October 2006

Abstract

Two second-order numerical schemes for von-Mises plasticity with a combination of linear isotropic and nonlinear kinematic hardening are presented. The first scheme is the generalized midpoint integration procedure, originally introduced by Ortiz and Popov in 1985, detailed and applied here to the case of Armstrong–Frederick nonlinear kinematic hardening. The second algorithm is based on the constitutive model exponential-based reformulation and on the integration procedure previously introduced by the authors in the context of linearly hardening materials. There are two main targets to the work. Firstly, we wish to extensively test the generalized midpoint procedure since in the scientific literature no thorough numerical testing campaign has been carried out on this second-order algorithm. Secondly, we wish to extend the exponential-based integration technique also to nonlinear hardening materials. A wide numerical investigation is carried out in order to compare the performance of the two methods.
© 2006 Elsevier B.V. All rights reserved.

Keywords: Plasticity; Exponential-based integration algorithm; Return map; Second-order method; Armstrong–Frederick constitutive model; Nonlinear kinematic hardening

1. Introduction

In the present paper we address the numerical solution algorithm for a von-Mises elastoplastic model with a combination of linear isotropic hardening and nonlinear Armstrong–Frederick kinematic hardening in the realm of small deformations [3].

The main aim of the present contribution is to develop and to test two second-order schemes for the aforementioned model. To the authors' knowledge, in the scientific literature, the issue on second-order accurate integration schemes which allow for nonlinear kinematic hardening is not studied, while a number of first-order accurate procedures are known [6,4,24].

The first numerical scheme considered here follows from the methods proposed in the work of Ortiz and Popov [15]. These methods adopt a single-step generalized midpoint integration rule for approximating the time derivatives and make use of a return map algorithm for the solution of the ensuing nonlinear algebraic system. Accordingly, the first method object of study is labeled MPTnl and represents a special case of generalized midpoint integration algorithm. This scheme shows yield consistency at the end of each step and is second-order accurate.

The second scheme introduced is based on a quasi-linear reformulation of the constitutive model combined with an exponential-based time integration method. The proposed integration scheme, labeled ESC^{2}nl, is achieved in the spirit of [2]. It is noted that exponential-based integration

* Corresponding author. Address: IMATI-CNR, Pavia, Via Ferrata 1, I-27100, Italy. Tel.: +39 0382 548229; fax: +39 0382 548300.
E-mail address: artioli@imati.cnr.it (E. Artioli).

0045-7825/$ - see front matter © 2006 Elsevier B.V. All rights reserved.
doi:10.1016/j.cma.2006.10.002

algorithms, although computationally more expensive than methods based on finite difference integration schemes and return map methods, exhibit second-order accuracy and high levels of precision.

In the present work we also consider the well known return map method based on backward Euler integration rule [4]. This scheme, labeled BEnl, is yield consistent and exhibits first-order accuracy.

The paper is organized as follows. In Section 2 we present the basic equations governing the plasticity model under consideration. In Section 3 we present the midpoint scheme MPTnl and the BEnl method. Section 4 is divided in two parts: first we propose a time continuous reformulation of the constitutive model and then we describe the ESC^{2}nl integration procedure based on exponential maps.

In Section 5 we develop extensive numerical tests in order to compare the considered methods, using the first-order accurate BEnl method to calculate reference solutions when needed. The numerical tests comprise pointwise mixed stress–strain histories, iso-error maps and an initial boundary value problem on a perforated strip.

Finally, after the conclusions of Section 6, in Appendix A we provide the derivation of the elastoplastic tangent operator consistent with the exponential-based algorithm introduced in Section 4.

Remark 1.1. In the sequel, we make the following use of the terms *accuracy* and *precision* as well as *accurate* and *precise*. With the terms accuracy and accurate we refer to the well known mathematical concept of numerical accuracy[1] [13,11]. Precision and precise are used in a more general fashion in order to indicate a comparison between different schemes in terms of error.

2. Time continuous model

We consider an associative von-Mises plasticity model with a combination of linear isotropic and nonlinear kinematic hardening in the realm of small deformations [4,25]. Splitting the strain and stress tensors, $\boldsymbol{\sigma}$ and $\boldsymbol{\varepsilon}$, in deviatoric and volumetric parts we have

$$\boldsymbol{\sigma} = \mathbf{s} + p\mathbf{I} \quad \text{with } p = \frac{1}{3}\mathrm{tr}(\boldsymbol{\sigma}), \tag{1}$$

$$\boldsymbol{\varepsilon} = \mathbf{e} + \frac{1}{3}\theta\mathbf{I} \quad \text{with } \theta = \mathrm{tr}(\boldsymbol{\varepsilon}), \tag{2}$$

where tr( ) indicates the trace operator, while $\mathbf{I}$, $\mathbf{s}$, p, $\mathbf{e}$, θ are respectively the second-order identity tensor, the deviatoric and volumetric stresses, the deviatoric and volumetric strains.

The equations for the model are

$$p = K\theta, \tag{3}$$

$$\mathbf{s} = 2G(\mathbf{e} - \mathbf{e}^{\mathrm{p}}), \tag{4}$$

$$\boldsymbol{\Sigma} = \mathbf{s} - \boldsymbol{\alpha}, \tag{5}$$

$$F = \|\boldsymbol{\Sigma}\| - \sigma_{\mathrm{y}}, \tag{6}$$

$$\dot{\mathbf{e}}^{\mathrm{p}} = \dot{\gamma}\mathbf{n}, \tag{7}$$

$$\sigma_{\mathrm{y}} = \sigma_{\mathrm{y},0} + H_{\mathrm{iso}}\gamma, \tag{8}$$

$$\dot{\boldsymbol{\alpha}} = H_{\mathrm{kin}}\dot{\gamma}\mathbf{n} - H_{\mathrm{nl}}\dot{\gamma}\boldsymbol{\alpha}, \tag{9}$$

$$\dot{\gamma} \geqslant 0, \quad F \leqslant 0, \quad \dot{\gamma}F = 0, \tag{10}$$

where K is the material bulk elastic modulus, G is the material shear modulus, $\mathbf{e}^{\mathrm{p}}$ is the traceless plastic strain, $\boldsymbol{\Sigma}$ is the relative stress in terms of the backstress $\boldsymbol{\alpha}$, the latter introduced to describe the kinematic hardening mechanism. Moreover, F is the von-Mises yield function, $\mathbf{n}$ is the normal to the yield surface, σ_{y_0} and σ_{y} are the initial and updated yield surface radii, while H_{iso}, H_{kin} and H_{nl} represent respectively the linear isotropic, linear kinematic and nonlinear kinematic hardening moduli. Finally, Eq. (10) are the Kuhn–Tucker conditions; in particular, the second equation limits the relative stress within the admissible region defined by the yield surface limit $F \leqslant 0$, while the other two are necessary to determine the plastic behavior. With a slight over-simplification of the model complexity, we may say that when $\dot{\gamma} = 0$ the system is in an elastic phase, while when $\dot{\gamma} > 0$ we say that the system is in a plastic phase.

Remark 2.1. Due to the linearity of the constitutive equations for the volumetric part of the constitutive model, the algorithms presented in the following sections refer only to the integration of the deviatoric part of the model.

3. Generalized midpoint integration algorithms

In this section we present the numerical method already proposed by Ortiz and Popov in 1985 [15] in the general framework of non-associative plasticity, specializing it to the particular model under consideration. The scheme is based on a generalized midpoint integration rule combined with a return map algorithm. The return map is achieved enforcing consistency at the end of the time step, which corresponds to projecting the trial solution onto the updated yield surface.

In particular, the generalized midpoint integration rule investigated by Ortiz and Popov can be applied to develop two different methods, namely the proper midpoint integration scheme [21] and the well known backward Euler integration scheme [4,18]. The first one is referred to as the MPTnl method (midpoint integration method for von-Mises plasticity with nonlinear hardening), while the

[1] Let s be the solution to the Cauchy problem

$$\dot{s}(t) = f(s,t), \quad t \in [0,T], \; s(0) = s_0$$

with f the driving load and s_0 the initial condition. Then, a numerical scheme applied to the above problem is said *accurate of order m* if it exists $C > 0$ such that, given any discrete time instants $0 \leqslant t_n < t_{n+1} \leqslant T$ and a set of (initial instant) data $\{s_n = s(t_n)\}$, it holds

$$(\Delta t)^{-1}\|s_{n+1} - s(t_{n+1})\| \leqslant C(\Delta t)^m$$

for sufficiently small $\Delta t = t_{n+1} - t_n$. The norm above is a fixed norm on the solution space, while s_{n+1} represents the (final instant) solution obtained with the numerical scheme.

second one is labeled BEnl (Backward-Euler integration method for von-Mises plasticity with nonlinear hardening). In this section, the above numerical methods are provided with their algorithmic solution sketch and elastoplastic consistent tangent operator.

To the authors' knowledge, the literature does not report any detailed development or testing of the midpoint method for the von-Mises plasticity model with nonlinear hardening as the one considered here.

In the sequel we assume that the time history interval $[0,T]$ is divided into N sub-intervals defined by the points $0=t_0<t_1<\cdots<t_n<t_{n+1}<\cdots<t_N=T$. For convenience, the generalized midpoint instant $t_{n+\alpha}$ is introduced here, such that $t_n\leqslant t_{n+\alpha}\leqslant t_{n+1}$ or, equivalently, such that the scalar parameter $\alpha\in[0,1]$. Focusing on a general time interval $[t_n,t_{n+1}]$ the problem under investigation may be stated as follows. Given the values of the history variables, namely the stress deviator and the internal variables $\{\mathbf{s}_n,\mathbf{e}_n,\mathbf{e}^{\mathrm{p}}_n,\gamma_n,\boldsymbol{\alpha}_n\}$ at time t_n and the deviatoric strain $\mathbf{e}_{n+1}$ at time t_{n+1}, compute the updated values $\{\mathbf{s}_{n+1},\mathbf{e}_{n+1},\mathbf{e}^{\mathrm{p}}_{n+1},\gamma_{n+1},\boldsymbol{\alpha}_{n+1}\}$ at time t_{n+1}. The strain history is assumed to be piecewise linear, while for simplicity the initial values of γ, $\mathbf{e}^{\mathrm{p}}$ and $\boldsymbol{\alpha}$ at time $t=0$ are taken zero.

3.1. Integration scheme

The used generalized midpoint integration rule for the evolutive Eqs. (7)–(9) leads to an integration scheme of the form

$$\begin{cases}\mathbf{e}^{\mathrm{p}}_{n+1}=\mathbf{e}^{\mathrm{p}}_n+\lambda\mathbf{n}_{n+\alpha},\\ \boldsymbol{\alpha}_{n+1}=\boldsymbol{\alpha}_n+\lambda(H_{\mathrm{kin}}\mathbf{n}_{n+\alpha}-H_{\mathrm{nl}}\boldsymbol{\alpha}_{n+\alpha}),\\ \mathbf{s}_{n+1}=2G(\mathbf{e}_{n+1}-\mathbf{e}^{\mathrm{p}}_{n+1}),\\ \boldsymbol{\Sigma}_{n+1}=\mathbf{s}_{n+1}-\boldsymbol{\alpha}_{n+1},\\ \gamma_{n+1}=\gamma_n+\lambda,\end{cases}\tag{11}$$

where λ represents the incremental plastic parameter to be determined enforcing the plastic consistency condition $F(\boldsymbol{\Sigma}_{n+1})\leqslant 0$. The quantities evaluated at the midpoint instant $t_{n+\alpha}$ are related to the corresponding values at t_n and t_{n+1} by a linear interpolation through the scalar α

$$\begin{cases}\mathbf{e}_{n+\alpha}=\alpha\mathbf{e}_{n+1}+(1-\alpha)\mathbf{e}_n,\\ \mathbf{e}^{\mathrm{p}}_{n+\alpha}=\alpha\mathbf{e}^{\mathrm{p}}_{n+1}+(1-\alpha)\mathbf{e}^{\mathrm{p}}_n,\\ \boldsymbol{\alpha}_{n+\alpha}=\alpha\boldsymbol{\alpha}_{n+1}+(1-\alpha)\boldsymbol{\alpha}_n,\\ \mathbf{s}_{n+\alpha}=2G(\mathbf{e}_{n+\alpha}-\mathbf{e}^{\mathrm{p}}_{n+\alpha}),\\ \boldsymbol{\Sigma}_{n+\alpha}=\mathbf{s}_{n+\alpha}-\boldsymbol{\alpha}_{n+\alpha}.\end{cases}\tag{12}$$

The scalar α can be arbitrarily chosen in the range $[0,1]$. In particular, in the following we consider two possibilities: $\alpha=1/2$, leading to the midpoint integration rule (MPTnl) and $\alpha=1$ leading to the backward Euler integration rule (BEnl). The choice $\alpha=1/2$ guarantees quadratic accuracy of the MPTnl method during purely plastic steps, while the choice $\alpha=1$ makes the BEnl method a simpler and more robust scheme with linear accuracy.

3.2. Solution algorithm

We initially suppose the step to be elastic and calculate trial values at the final stage t_{n+1}:

$$\begin{cases}\mathbf{e}^{\mathrm{p,TR}}_{n+1}=\mathbf{e}^{\mathrm{p}}_n,\\ \mathbf{s}^{\mathrm{TR}}_{n+1}=2G(\mathbf{e}_{n+1}-\mathbf{e}^{\mathrm{p}}_n),\\ \boldsymbol{\alpha}^{\mathrm{TR}}_{n+1}=\boldsymbol{\alpha}_n,\\ \boldsymbol{\Sigma}^{\mathrm{TR}}_{n+1}=\mathbf{s}^{\mathrm{TR}}_{n+1}-\boldsymbol{\alpha}^{\mathrm{TR}}_{n+1},\\ \gamma^{\mathrm{TR}}_{n+1}=\gamma_n.\end{cases}\tag{13}$$

If the resulting stress is admissible, i.e.

$$\|\boldsymbol{\Sigma}^{\mathrm{TR}}_{n+1}\|\leqslant\sigma_{\mathrm{y},0}+H_{\mathrm{iso}}\gamma^{\mathrm{TR}}_{n+1}\tag{14}$$

the "whole" step is assumed to be elastic and the variable values at the final time instant are taken as the trial ones. On the other hand, if $\boldsymbol{\Sigma}^{\mathrm{TR}}_{n+1}$ violates the yield limit, a plastic correction is introduced in two steps:

- STEP 1: update at $t_{n+\alpha}$.

$$\begin{cases}\boldsymbol{\alpha}_{n+\alpha}=V^{\lambda}\boldsymbol{\alpha}^{\mathrm{TR}}_{n+1}+\alpha H_{\mathrm{kin}}V^{\lambda}\lambda\mathbf{n}_{n+\alpha},\\ \mathbf{s}_{n+\alpha}=\mathbf{s}^{\mathrm{TR}}_{n+\alpha}-2G\alpha\lambda\mathbf{n}_{n+\alpha},\\ \boldsymbol{\Sigma}_{n+\alpha}=\mathbf{s}_{n+\alpha}-\boldsymbol{\alpha}_{n+\alpha},\end{cases}\tag{15}$$

  where

$$\mathbf{s}^{\mathrm{TR}}_{n+\alpha}=2G(\mathbf{e}_{n+\alpha}-\mathbf{e}^{\mathrm{p}}_n),$$
$$V^{\lambda}=\frac{1}{1+\alpha H_{\mathrm{nl}}\lambda}.$$

- STEP 2: update at t_{n+1}.

$$\begin{cases}\mathbf{e}^{\mathrm{p}}_{n+1}=\mathbf{e}^{\mathrm{p}}_n+\lambda\mathbf{n}_{n+\alpha},\\ \boldsymbol{\alpha}_{n+1}=W^{\lambda}\boldsymbol{\alpha}_n+H_{\mathrm{kin}}V^{\lambda}\lambda\mathbf{n}_{n+\alpha},\\ \mathbf{s}_{n+1}=2G(\mathbf{e}_{n+1}-\mathbf{e}^{\mathrm{p}}_{n+1}),\\ \boldsymbol{\Sigma}_{n+1}=\mathbf{s}_{n+1}-\boldsymbol{\alpha}_{n+1},\\ \gamma_{n+1}=\gamma_n+\lambda\end{cases}\tag{16}$$

  with

$$W^{\lambda}=\frac{1+(\alpha-1)\lambda H_{\mathrm{nl}}}{1+\alpha\lambda H_{\mathrm{nl}}}.$$

Remark 3.1. In the case of the BEnl scheme, step (16) is equivalent to (15) and can be avoided in the procedure.

It is noted that in Eqs. (15) and (16) the only unknown is represented by the plastic rate parameter λ which is computed enforcing the yield consistency condition at t_{n+1}. Observing that $(15)_3$ can be rewritten as

$$\boldsymbol{\Sigma}_{n+\alpha}=\boldsymbol{\Sigma}^{\lambda}_B-Y^{\lambda}\mathbf{n}_{n+\alpha}\tag{17}$$

with

$$\boldsymbol{\Sigma}^{\lambda}_B=\mathbf{s}^{\mathrm{TR}}_{n+\alpha}-V^{\lambda}\boldsymbol{\alpha}^{\mathrm{TR}}_{n+1},$$
$$Y^{\lambda}=2G\alpha\lambda+\alpha H_{\mathrm{kin}}V^{\lambda}\lambda,$$

we may conclude that $\boldsymbol{\Sigma}_{n+\alpha}$ and $\boldsymbol{\Sigma}^{\lambda}_B$ are parallel i.e.

$$\|\boldsymbol{\Sigma}_{n+\alpha}\|=\|\boldsymbol{\Sigma}^{\lambda}_B\|-Y^{\lambda}.\tag{18}$$

Using relation (18) we can finally write the yield consistency condition at t_{n+1} as follows

$$\|\boldsymbol{\Sigma}_{n+1}\| = \left\| \frac{1}{\alpha}\boldsymbol{\Sigma}_{n+\alpha} - \left(\frac{1-\alpha}{\alpha}\right)\boldsymbol{\Sigma}_n \right\| = \sigma_{y,n} + \lambda H_{\text{iso}}. \tag{19}$$

We are therefore interested in the minimum positive root of the nonlinear equation (19), which, squaring both members becomes

$$\frac{1}{\alpha^2}\|\boldsymbol{\Sigma}_{n+\alpha}\|^2 - 2\left(\frac{1-\alpha}{\alpha^2}\right)(\boldsymbol{\Sigma}_{n+\alpha} : \boldsymbol{\Sigma}_n) + \left(\frac{1-\alpha}{\alpha}\right)^2 \|\boldsymbol{\Sigma}_n\|^2 - (\sigma_{y,n} + \lambda H_{\text{iso}})^2 = 0 \tag{20}$$

a rational fractional polynomial in λ. With some algebra (20) can be transformed into a non-fractional 10th degree polynomial in λ whose minimum positive root is then sought for with an iterative numerical method. In the present implementation of the MPTnl scheme, use is made of the DZPLRC subroutine suitable for finding the zeroes of a polynomial with real coefficients using Laguerre's method [10].

Remark 3.2. In the case of the BEnl scheme, Eq. (20) takes a simpler form as the second and third term in the left hand side vanish. As a consequence, the resulting left hand side in (20) reduces to a fourth degree polynomial in λ with much shorter coefficients than those corresponding to the MPTnl scheme [4].

Remark 3.3. Both schemes here presented are yield consistent. Regarding instead the order of accuracy, the BEnl method is *linear* while the MPTnl method is *quadratic*.

3.3. Elastoplastic consistent tangent operators

We present here the elastoplastic tangent operators consistent with the MPTnl and the BEnl scheme, respectively. For brevity's sake, we just report the final form of the operators for an elastoplastic step (i.e. such that $\lambda \neq 0$) without deriving it thoroughly. To make notation more clear, the subscripts of all history variables evaluated at time t_{n+1} are omitted for brevity, while quantities evaluated either at t_n or at $t_{n+\alpha}$ are specified by the relative subscript.

3.3.1. MPTnl method

Following a classical derivation procedure [15,20,4], the consistent tangent operator $\partial\boldsymbol{\sigma}/\partial\boldsymbol{\varepsilon}$ for the MPTnl scheme is obtained. We first recall that

$$\frac{\partial \mathbf{s}}{\partial \boldsymbol{\varepsilon}} = \frac{\partial \mathbf{s}}{\partial \mathbf{e}}\frac{\partial \mathbf{e}}{\partial \boldsymbol{\varepsilon}} = \frac{\partial \mathbf{s}}{\partial \mathbf{e}}\mathbb{I}_{\text{dev}}, \tag{21}$$

where

$$\mathbb{I}_{\text{dev}} = \mathbb{I} - \frac{1}{3}(\mathbf{I}\otimes\mathbf{I}) \tag{22}$$

and $\mathbb{I}$ is the fourth-order identity tensor. Taking into account the volumetric part of the stress, from Eqs. (1)–(3) we get

$$\mathbb{D}_{\text{disc}} = \frac{\partial \boldsymbol{\sigma}}{\partial \boldsymbol{\varepsilon}} = \frac{\partial \mathbf{s}}{\partial \mathbf{e}}\mathbb{I}_{\text{dev}} + K(\mathbf{I}\otimes\mathbf{I}). \tag{23}$$

The fourth-order tensor $\frac{\partial \mathbf{s}}{\partial \mathbf{e}}$ can be computed as

$$\frac{\partial \mathbf{s}}{\partial \mathbf{e}} = \mathbb{M}_1 + \mathbb{M}_2, \tag{24}$$

where $\mathbb{M}_1$ and $\mathbb{M}_2$ are given by the following expressions

$$\mathbb{M}_1 = 2G\left(\mathbb{I} - \eta\mathbb{I}_{\mathbf{n}} - \mathbf{n}_{n+\alpha}\otimes\frac{\partial\lambda}{\partial\mathbf{e}}\right), \tag{25}$$

$$\mathbb{M}_2 = \eta\mathbb{I}_{\mathbf{n}}\left(\boldsymbol{\beta}\otimes\frac{\partial\lambda}{\partial\mathbf{e}}\right) \tag{26}$$

with

$$\eta = \lambda\frac{2G + H_{\text{kin}}V^{\lambda}}{2G\lambda + H_{\text{kin}}V^{\lambda}\lambda + 2\|\boldsymbol{\Sigma}_{n+\alpha}\|}, \tag{27}$$

$$\mathbb{I}_{\mathbf{n}} = \mathbb{I} - \mathbf{n}_{n+\alpha}\otimes\mathbf{n}_{n+\alpha}, \tag{28}$$

$$\frac{\partial\lambda}{\partial\mathbf{e}} = -2G(\theta_1+\theta_2)^{-1}\left(\mathbb{I} - \frac{2G\lambda + H_{\text{kin}}V^{\lambda}\lambda/2}{2\|\mathbf{s}^{\text{TR}}_{n+\alpha} - V^{\lambda}\boldsymbol{\alpha}_n\|}\mathbb{I}_{\mathbf{n}}\right)\boldsymbol{\Sigma}, \tag{29}$$

$$\theta_1 = H_{\text{iso}}\sigma_{y,n+1} + (\boldsymbol{\beta} + 2G\mathbf{n}_{n+\alpha}) : \boldsymbol{\Sigma}, \tag{30}$$

$$\theta_2 = \frac{H_{\text{nl}}(2G\lambda + H_{\text{kin}}V^{\lambda}\lambda/2)}{2(V^{\lambda})^2}\frac{(\boldsymbol{\Sigma} : \mathbb{I}_{\mathbf{n}}\boldsymbol{\alpha}_n)}{\|\mathbf{s}^{\text{TR}}_{n+\alpha} - V^{\lambda}\boldsymbol{\alpha}_n\|}, \tag{31}$$

$$\boldsymbol{\beta} = \frac{1}{2}\frac{H_{\text{nl}}}{(V^{\lambda})^2}\boldsymbol{\alpha}_n - \left[\frac{1}{4}H_{\text{kin}}\frac{\lambda H_{\text{nl}}}{(V^{\lambda})^2} + \frac{1}{2}H_{\text{kin}}V^{\lambda}\right]\mathbf{n}_{n+\alpha}. \tag{32}$$

3.3.2. BEnl method

The elastoplastic consistent tangent operator for the BEnl method can be obtained from (23) setting $\alpha = 1$ in Eqs. (25)–(32). On the other hand, the easier form of the BEnl algorithm allows a direct computation; the reader is referred to [4] for a complete derivation of this step.

3.4. Some points on the BEnl and MPTnl algorithms numerical properties

- Regarding the issue of stability, to the authors' knowledge, no result is present in the literature for the present non-associative model. On the other hand, the backward Euler scheme is proved to be B-stable for the case with linear hardening in [17,18]. Regarding the midpoint scheme with endpoint consistency, only a weaker stability result, valid for purely plastic loading histories, is proved in [15] for the same model with linear hardening.
- It is well known that, as the time step size increases, the backward Euler method behaves progressively better than the midpoint scheme. This observation can be clearly appreciated considering the case of von-Mises perfect plasticity; differently from the backward Euler scheme, the midpoint method is unable to mimic the behavior of the exact solution for infinitely long time steps (see for example [18,19]).

- For the present model, the MPTnl scheme here detailed is not guaranteed to have a solution for every trial $\mathbf{s}_{n+1}^{\mathrm{TR}}$ [15]. On the other hand, from all the numerical tests carried out, it seems that a solution always exists for reasonable values of strain increment $\|\Delta\mathbf{e}\|$.
- Finally, the reader should be aware that the extension of the midpoint integration method to more general yield surfaces is more complicated than for the simpler backward Euler scheme. In particular, one of the main difficulties is related to finding the stress projection point on the yield surface.

4. An exponential-based integration algorithm

In this section we present the second numerical scheme addressed in the paper. This method is based on an ad-hoc rewriting of the time continuous model and on the application of exponential maps for the integration of the respective dynamical system. A continuous reformulation following a similar philosophy has been considered also in other contributions, see for example [7,9,8,14] and references therein. The new algorithm here presented, referred as ESC^{2}nl, represents an extension of previous algorithms introduced by the authors in the case of von-Mises plasticity with linear hardening [1,2] and it belongs to a family of integration schemes labeled "ESC".

4.1. A model reformulation

Combining Eqs. (4) and (5), we obtain

$$\boldsymbol{\Sigma} + \boldsymbol{\alpha} + 2G\mathbf{e}^{\mathrm{p}} = 2G\mathbf{e}, \tag{33}$$

which taking the derivative in time, applying Eqs. (7) and (9) and rearranging terms gives

$$\dot{\boldsymbol{\Sigma}} = 2G\dot{\mathbf{e}} - (2G + H_{\mathrm{kin}})\dot{\mathbf{e}}^{\mathrm{p}} + H_{\mathrm{nl}}\dot{\gamma}\boldsymbol{\alpha}. \tag{34}$$

Now, recalling the yield surface radius

$$\sigma_{\mathrm{y}} = \sigma_{\mathrm{y},0} + H_{\mathrm{iso}}\gamma \tag{35}$$

and that in the plastic phase ($\dot{\gamma} > 0$)

$$\mathbf{n} = \frac{\boldsymbol{\Sigma}}{\|\boldsymbol{\Sigma}\|} = \frac{\boldsymbol{\Sigma}}{\sigma_{\mathrm{y},0} + H_{\mathrm{iso}}\gamma} = \frac{\boldsymbol{\Sigma}}{\sigma_{\mathrm{y}}}, \tag{36}$$

we may apply (7) in (34) obtaining

$$\dot{\boldsymbol{\Sigma}} + (2G + H_{\mathrm{kin}})\frac{\boldsymbol{\Sigma}}{\sigma_{\mathrm{y}}}\dot{\gamma} = 2G\dot{\boldsymbol{\Psi}}, \tag{37}$$

where we introduced the position

$$\dot{\boldsymbol{\Psi}} = \dot{\mathbf{e}} + \frac{H_{\mathrm{nl}}}{2G}\dot{\gamma}\boldsymbol{\alpha}. \tag{38}$$

Note that (37) is a differential equation for $\boldsymbol{\Sigma}$ that is valid also during elastic phases ($\dot{\gamma} = 0$). Introducing the *scaled relative stress*

$$\overline{\boldsymbol{\Sigma}} := \frac{\boldsymbol{\Sigma}}{\sigma_{\mathrm{y}}}, \tag{39}$$

we observe that, whenever the relative stress $\boldsymbol{\Sigma}$ lies on the yield surface, then $\overline{\boldsymbol{\Sigma}} = \mathbf{n}$, while this is not true when $\boldsymbol{\Sigma}$ lays inside the yield surface. The time derivative of (39) and the use of relation (35) gives

$$\dot{\overline{\boldsymbol{\Sigma}}} = \frac{\dot{\boldsymbol{\Sigma}}}{\sigma_{\mathrm{y}}} - \frac{H_{\mathrm{iso}}}{\sigma_{\mathrm{y}}}\dot{\gamma}\overline{\boldsymbol{\Sigma}}. \tag{40}$$

Using Eqs. (37) and (40), one obtains

$$\dot{\overline{\boldsymbol{\Sigma}}} + \frac{2G + H_{\mathrm{kin}} + H_{\mathrm{iso}}}{\sigma_{\mathrm{y}}}\dot{\gamma}\overline{\boldsymbol{\Sigma}} = \frac{2G}{\sigma_{\mathrm{y}}}\dot{\boldsymbol{\Psi}}. \tag{41}$$

The next goal is to introduce a scalar *integration factor* X_0 for the above evolutionary equation. In other words, we search for a scalar function depending on time X_0 such that

$$X_0\dot{\overline{\boldsymbol{\Sigma}}} + X_0\frac{2G + H_{\mathrm{kin}} + H_{\mathrm{iso}}}{\sigma_{\mathrm{y}}}\dot{\gamma}\overline{\boldsymbol{\Sigma}} = \frac{\mathrm{d}}{\mathrm{d}t}[X_0\overline{\boldsymbol{\Sigma}}]. \tag{42}$$

Multiplying Eq. (41) by X_0, one obtains

$$\frac{\mathrm{d}}{\mathrm{d}t}[X_0\overline{\boldsymbol{\Sigma}}] = \frac{2G}{\sigma_{\mathrm{y}}}X_0\dot{\boldsymbol{\Psi}}. \tag{43}$$

Accordingly, we set

$$X_0(\gamma) = \begin{cases} \left(1 + \dfrac{\gamma H_{\mathrm{iso}}}{\sigma_{\mathrm{y},0}}\right)^{\frac{2G + H_{\mathrm{kin}} + H_{\mathrm{iso}}}{H_{\mathrm{iso}}}} & \text{if } H_{\mathrm{iso}} \neq 0, \\ \exp\left(\dfrac{2G + H_{\mathrm{kin}} + H_{\mathrm{iso}}}{\sigma_{\mathrm{y},0}}\gamma\right) & \text{if } H_{\mathrm{iso}} = 0. \end{cases} \tag{44}$$

Noting that such a function is continuous for fixed γ and $H_{\mathrm{iso}} \to 0$ and that

$$\dot{X}_0 = \frac{2G + H_{\mathrm{kin}} + H_{\mathrm{iso}}}{\sigma_{\mathrm{y}}}\dot{\gamma}X_0, \tag{45}$$

we immediately obtain relationship (42) and therefore (43).

We now need an evolution law for X_0. In elastic phases, such law follows immediately from (45):

$$\dot{X}_0 = 0 \quad \text{(elastic phases)}. \tag{46}$$

On the other hand, for $\dot{\gamma} \neq 0$, taking the scalar product of (43) with $\overline{\boldsymbol{\Sigma}}$, we have

$$X_0\frac{1}{2}\frac{\mathrm{d}}{\mathrm{d}t}\|\overline{\boldsymbol{\Sigma}}\|^2 + \dot{X}_0\|\overline{\boldsymbol{\Sigma}}\|^2 = \frac{2G}{\sigma_{\mathrm{y}}}X_0\dot{\boldsymbol{\Psi}} : \overline{\boldsymbol{\Sigma}}, \tag{47}$$

which, noting that in plastic phases

$$\|\overline{\boldsymbol{\Sigma}}\| = \frac{\|\boldsymbol{\Sigma}\|}{\sigma_{\mathrm{y}}} = 1 \tag{48}$$

and using (47) gives

$$\dot{X}_0 = \frac{2G}{\sigma_{\mathrm{y}}}\dot{\boldsymbol{\Psi}} : X_0\overline{\boldsymbol{\Sigma}} \quad \text{(plastic phases)}. \tag{49}$$

Defining the tensor

$$\mathbf{X}^s = X_0\overline{\boldsymbol{\Sigma}}. \tag{50}$$

Eq. (43) can be rewritten as

$$\dot{\mathbf{X}}^s = \frac{2G}{\sigma_{\mathrm{y}}}X_0\dot{\boldsymbol{\Psi}}, \tag{51}$$

while (49) becomes

$$\dot{X}_0 = \frac{2G}{\sigma_y}\dot{\boldsymbol{\Psi}} : \mathbf{X}^s \quad \text{(plastic phases)}. \tag{52}$$

At this stage, we introduce the *generalized stress* $\mathbf{X}$ as the couple

$$\mathbf{X} = \begin{pmatrix} X_0\overline{\boldsymbol{\Sigma}} \\ X_0 \end{pmatrix} = \begin{pmatrix} \mathbf{X}^s \\ X_0 \end{pmatrix} \tag{53}$$

and we consider a linear space structure on the space of generalized stresses, the product by a scalar and the sum between couples being defined in the obvious natural way. Moreover, any element of the space of linear operators from the generalized stress space into itself can be written as

$$\mathbb{M} = \begin{pmatrix} \mathbb{M}_{11} & \mathbf{M}_{12} \\ \mathbf{M}_{21} & M_{22} \end{pmatrix} \tag{54}$$

with $\mathbb{M}_{11}$ a fourth-order tensor, $\mathbf{M}_{12}$, $\mathbf{M}_{21}$ second-order tensors and M_{22} a scalar, under the convention that

$$\mathbb{M}\mathbf{Y} = \begin{pmatrix} \mathbb{M}_{11} & \mathbf{M}_{12} \\ \mathbf{M}_{21} & M_{22} \end{pmatrix}\begin{pmatrix} \mathbf{Y}^s \\ Y_0 \end{pmatrix} = \begin{pmatrix} \mathbb{M}_{11} : \mathbf{Y}^s + \mathbf{M}_{12}Y_0 \\ \mathbf{M}_{21} : \mathbf{Y}^s + M_{22}Y_0 \end{pmatrix} \tag{55}$$

for any couple $\mathbf{Y} = (\mathbf{Y}^s, Y_0)^{\mathrm{T}}$ in the generalized stress space. In the sequel, we consider a linear space structure also on the space of the linear operators acting on couples, again with the product by a scalar and the sum between such linear operators being defined in the obvious natural way.

Eqs. (51), (46) and (52) provide a system for the *generalized stress vector* $\mathbf{X}$, in the form

$$\dot{\mathbf{X}} = \mathbb{A}\mathbf{X}, \tag{56}$$

where $\mathbb{A}$ represents a linear operator acting from the space of couples into itself, and depending on the actual phase as follows

$$\mathbb{A} = \mathbb{A}_e = \frac{2G}{\sigma_y}\begin{pmatrix} \mathbb{O} & \dot{\boldsymbol{\Psi}} \\ \mathbf{0} & 0 \end{pmatrix} \quad \text{(elastic phase)}, \tag{57}$$

$$\mathbb{A} = \mathbb{A}_p = \frac{2G}{\sigma_y}\begin{pmatrix} \mathbb{O} & \dot{\boldsymbol{\Psi}} \\ \dot{\boldsymbol{\Psi}} & 0 \end{pmatrix} \quad \text{(plastic phase)}, \tag{58}$$

where $\mathbf{0}$ and $\mathbb{O}$ indicate respectively the second-order and fourth-order null tensors.

Expression (56) is a formal compact notation to describe the action of the linear operator $\mathbb{A}$ on the couple $\mathbf{X}$, as introduced in (55).

Therefore the original problem, expressed by Eqs. (4)–(9), is substituted by a new one, expressed by Eqs. (56)–(58). Note that $\dot{\boldsymbol{\Psi}}$ can be equivalently substituted by $\dot{\mathbf{e}}$ in (57), because $\dot{\gamma} = 0$ during elastic phases.

Remark 4.1. Unless $H_{\mathrm{iso}} = H_{\mathrm{nl}} = 0$, the operator $\mathbb{A}$ is not constant in time, therefore our formulation (56) is nonlinear. Anyway, the particular form of the dynamical system (56) is indeed of great value, allowing us to develop the numerical method of Section 4.2.

4.1.1. Time-continuous on–off switch

To properly convert the original problem in a new but equivalent differential algebraic format, we also need to introduce an elastic/plastic phase determination criterion expressed in the new generalized stress environment.

For a given state to be plastic, the following two conditions must be fulfilled:

(1) The relative stress $\boldsymbol{\Sigma}$ must be on the yield surface, i.e.

$$\|\boldsymbol{\Sigma}\| = \sigma_y. \tag{59}$$

Using (39) and (53) this can be easily rewritten as

$$\|\mathbf{X}^s\|^2 = \|\overline{\boldsymbol{\Sigma}}\|^2 X_0^2 = \frac{\|\boldsymbol{\Sigma}\|^2}{\sigma_y^2}X_0^2 = X_0^2. \tag{60}$$

(2) The direction of the strain rate $\dot{\mathbf{e}}$ must be outward with respect to the yield surface, i.e.

$$\boldsymbol{\Sigma} : \dot{\mathbf{e}} > 0. \tag{61}$$

Again recalling (39) and (53) it is immediate to check that (61) is equivalent to

$$\mathbf{X}^s : \dot{\mathbf{e}} > 0. \tag{62}$$

If the two conditions (60) and (62) are not satisfied, the step is elastic.

4.2. Integration scheme

We assume as in Section 3 that the time history interval $[0, T]$ is divided into N sub-intervals defined by the points $0 = t_0 < t_1 < \cdots < t_n < t_{n+1} < \cdots < t_N = T$. Given the history variables $\{\mathbf{s}_n, \mathbf{e}_n, \mathbf{e}_n^{\mathrm{p}}, \gamma_n, \boldsymbol{\alpha}_n\}$ at time t_n and the deviatoric strain $\mathbf{e}_{n+1}$ at time t_{n+1}, we search for the updated variables at time t_{n+1}. As usual, the strain history is assumed to be piecewise linear, i.e. $\dot{\mathbf{e}}$ is constant within each time interval. Moreover, we assume to start from an unstressed and undeformed state, i.e. characterized by zero initial values of the variables γ, $\mathbf{e}^{\mathrm{p}}$ and $\boldsymbol{\alpha}$. Accordingly, the initial *generalized stress* is

$$\mathbf{X}_0 = \begin{pmatrix} \boldsymbol{\Sigma}_0/\sigma_{y,0} \\ 1 \end{pmatrix}. \tag{63}$$

Referring to the dynamical law (56) with the operator $\mathbb{A}$ given respectively by (57) or (58), we aim to derive a numerical scheme for the discrete evolution of $\mathbf{X}$ along the general time step $[t_n, t_{n+1}]$.

It is immediate to observe that, if during the time interval $[t_n, t_{n+1}]$ the material behavior is purely elastic ($\dot{\gamma} = 0$ – elastic step), then the operator $\mathbb{A}_e$ is constant within this interval. In this case, the dynamical equation (56) can be solved in closed form and the numerical scheme returns the exact solution. In analogy to (56), the discrete evolution of the generalized stress takes the expression

$$\mathbf{X}_{n+1} = \exp[\overline{\mathbb{A}}\Delta t]\mathbf{X}_n \tag{64}$$

with $\overline{\mathbb{A}} = \mathbb{A}_e$ and $\Delta t = t_{n+1} - t_n$. Note that, being $\overline{\mathbb{A}}$ an element in the linear space of linear operators acting on couples, the exponential of $\overline{\mathbb{A}}\Delta t$ is naturally defined by the (converging) exponential series

$$\overline{\mathbb{G}} = \exp[\overline{\mathbb{A}}\Delta t] = \sum_{n=0}^{+\infty} \frac{(\overline{\mathbb{A}}\Delta t)^n}{n!}. \tag{65}$$

Instead, if during the step $[t_n, t_{n+1}]$ purely plastic loading takes place, the linear operator $\mathbb{A}_p$ is not constant in time; in fact the yield surface radius σ_y and the "driving" tensor $\dot{\boldsymbol{\Psi}}$ cannot be expected to be constant whenever $\dot{\gamma} > 0$ (see Eqs. (8) and (38)). In such cases, therefore, the discrete solution of the dynamical system (56) is approximated by assuming that the above variables σ_y and $\dot{\boldsymbol{\Psi}}$ remain constant within the time step. As a consequence, an equation identical to (64) still holds, clearly with a different choice of $\overline{\mathbb{A}}$. This is equivalent to substitute the operator $\mathbb{A}_p$ with an operator $\overline{\mathbb{A}}_p$ which is constant during the time step. The respective constant values taken by σ_y and $\dot{\boldsymbol{\Psi}}$, which depend on known quantities evaluated at the beginning of the step t_n, are indicated by $\bar{\sigma}_y$ and $\overline{\dot{\boldsymbol{\Psi}}}$; we will specialize such constants in the immediate following. Note that different choices for $\bar{\sigma}_y$ and $\overline{\dot{\boldsymbol{\Psi}}}$ are possible, leading to different possible approximations and solution schemes. Therefore, the operator $\overline{\mathbb{A}}$ is specialized as

$$\overline{\mathbb{A}}_e = \frac{2G}{\sigma_{y,n}} \begin{pmatrix} \mathbb{O} & \dot{\mathbf{e}}_n \\ \mathbf{0} & 0 \end{pmatrix} \quad \text{(elastic step)} \tag{66}$$

and

$$\overline{\mathbb{A}}_p = \frac{2G}{\bar{\sigma}_y} \begin{pmatrix} \mathbb{O} & \overline{\dot{\boldsymbol{\Psi}}} \\ \overline{\dot{\boldsymbol{\Psi}}} & 0 \end{pmatrix} \quad \text{(plastic step)}, \tag{67}$$

respectively for an elastic and a plastic step. It is then possible to approximate equation (56)–(64). The operators $\overline{\mathbb{A}}_e\Delta t$ and $\overline{\mathbb{A}}_p\Delta t$ are by definition equal to the operators (57) and (58), respectively, after substituting $\dot{\boldsymbol{\Psi}}$ with $\Delta\overline{\boldsymbol{\Psi}} = \Delta t\overline{\dot{\boldsymbol{\Psi}}}$ and σ_y with $\bar{\sigma}_y$.

The choice of the parameters $\bar{\sigma}_y$ and $\overline{\dot{\boldsymbol{\Psi}}}$ for plastic steps is now addressed with emphasis on the effects this choice induces on the algorithmical properties. A possibility is given by the following values

$$\begin{cases} \bar{\sigma}_y = \dfrac{c\sigma_{y,n}}{\ln(1+c)}, \\ \Delta\overline{\boldsymbol{\Psi}} = \Delta t\overline{\dot{\boldsymbol{\Psi}}} = \Delta\overline{\boldsymbol{\Psi}}_0 + \Delta\overline{\boldsymbol{\Psi}}_1, \end{cases} \tag{68}$$

where the constant and the tensors appearing in (68) are given by

$$c = \frac{2G\bar{q}(\mathbf{n}_n : \Delta\mathbf{e})}{\sigma_{y,n}}, \tag{69}$$

$$\Delta\overline{\boldsymbol{\Psi}}_0 = \Delta\mathbf{e} + \frac{H_{nl}(\mathbf{n}_n : \Delta\mathbf{e})}{2G_1 - H_{nl}(\mathbf{n}_n : \boldsymbol{\alpha}_n)}\boldsymbol{\alpha}_n, \tag{70}$$

$$\Delta\overline{\boldsymbol{\Psi}}_1 = \frac{1}{2}\frac{H_{nl}}{2G}(\mathbf{D}_{\boldsymbol{\alpha}}D_\gamma + D'_\gamma\boldsymbol{\alpha}_n) \tag{71}$$

with

$$\begin{aligned}
&\Delta\mathbf{e} = \dot{\mathbf{e}}\Delta t = \mathbf{e}_{n+1} - \mathbf{e}_n, \\
&\bar{q} = \frac{H_{iso}}{2G_1 - H_{nl}(\mathbf{n}_n : \boldsymbol{\alpha}_n)}, \\
&\mathbf{n}_n = \frac{\mathbf{X}^s_n}{X_{0,n}}, \\
&2G_1 = 2G + H_{iso} + H_{kin}, \\
&D_\gamma = \frac{2G}{2G_1 - H_{nl}(\mathbf{n}_n : \boldsymbol{\alpha}_n)}(\mathbf{n}_n : \Delta\mathbf{e}), \\
&\mathbf{D}_{\boldsymbol{\alpha}} = (H_{kin}\mathbf{n}_n - H_{nl}\boldsymbol{\alpha})D_\gamma, \\
&D'_\gamma = \frac{2G}{2G_1 - H_{nl}(\mathbf{n}_n : \boldsymbol{\alpha}_n)}(\mathbf{D}_{\mathbf{n}} : \Delta\mathbf{e}) \\
&\qquad + \frac{H_{nl}D_\gamma}{2G_1 - H_{nl}(\mathbf{n}_n : \boldsymbol{\alpha}_n)}[(\mathbf{D}_{\mathbf{n}} : \boldsymbol{\alpha}_n) + (\mathbf{n}_n : \mathbf{D}_{\boldsymbol{\alpha}})], \\
&\mathbf{D}_{\mathbf{n}} = \frac{2G}{\sigma_{y,n}}\Delta\mathbf{e} - \frac{2G_1D_\gamma}{\sigma_{y,n}}\mathbf{n}_n + \frac{H_{nl}D_\gamma}{\sigma_{y,n}}\mathbf{D}_{\boldsymbol{\alpha}}.
\end{aligned}$$

The choice for $\bar{\sigma}_y$ in (68) corresponds to an extension of the ESC[2] scheme already proposed by the authors in [2]. Instead, the value for $\Delta\overline{\boldsymbol{\Psi}}$ is essentially derived from a first-order expansion of the tensor $\dot{\boldsymbol{\Psi}}$ in time. This choice guarantees a second-order scheme as well as other properties as discussed in the sequel.

The linear operator $\overline{\mathbb{G}}$ appearing in equation (65) can be calculated explicitly. Note that, for such a purpose, it is convenient to reformulate the linear operator $\overline{\mathbb{A}}\Delta t$ as a $\mathbb{R}^{7\times7}$ matrix, calculate the exponential and finally write it back in the original form (54). Without showing the calculations, we get

$$\overline{\mathbb{G}} = \begin{cases} \overline{\mathbb{G}}_e = \begin{pmatrix} \mathbb{I} & \dfrac{2G}{\bar{\sigma}_y}\Delta\mathbf{e} \\ \mathbf{0} & 1 \end{pmatrix} \quad \text{(elastic step)}, \\ \overline{\mathbb{G}}_p = \begin{pmatrix} \mathbb{I} + \left[\dfrac{(a-1)}{\|\Delta\overline{\boldsymbol{\Psi}}\|^2}\right]\Delta\overline{\boldsymbol{\Psi}}\otimes\Delta\overline{\boldsymbol{\Psi}} & b\dfrac{\Delta\overline{\boldsymbol{\Psi}}}{\|\Delta\overline{\boldsymbol{\Psi}}\|} \\ b\dfrac{\Delta\overline{\boldsymbol{\Psi}}^T}{\|\Delta\overline{\boldsymbol{\Psi}}\|} & a \end{pmatrix} \quad \text{(plastic step)}, \end{cases} \tag{72}$$

where the scalars a and b are

$$a = \cosh\left(\frac{2G}{\bar{\sigma}_y}\|\Delta\overline{\boldsymbol{\Psi}}\|\right), \tag{73}$$

$$b = \sinh\left(\frac{2G}{\bar{\sigma}_y}\|\Delta\overline{\boldsymbol{\Psi}}\|\right). \tag{74}$$

Another point to be addressed is the update of the backstress tensor $\boldsymbol{\alpha}$. Due to the presence of the nonlinear kinematic hardening in the model, the tensor $\boldsymbol{\alpha}(t)$ is not a function of $\mathbf{e}(t)$ and $\boldsymbol{\Sigma}(t)$, $t \in [0, T]$, but must be recorded separately. As a consequence, the backstress $\boldsymbol{\alpha}$ needs to be updated at all time steps. An approximated integration in time of Eq. (9) gives

$$\boldsymbol{\alpha}_{n+1} - \boldsymbol{\alpha}_n = \int_{t_n}^{t_{n+1}} (H_{\mathrm{kin}}\dot{\gamma}\mathbf{n} - H_{\mathrm{nl}}\dot{\gamma}\boldsymbol{\alpha})\,\mathrm{d}t \simeq \frac{\Delta\gamma}{2}[H_{\mathrm{kin}}(\mathbf{n}_{n+1}+\mathbf{n}_n) - H_{\mathrm{nl}}(\boldsymbol{\alpha}_{n+1}+\boldsymbol{\alpha}_n)]. \tag{75}$$

From Eq. (75) we get immediately

$$\boldsymbol{\alpha}_{n+1} \simeq \frac{H_{\mathrm{kin}}\Delta\gamma(\mathbf{n}_{n+1}+\mathbf{n}_n)/2 + (1 - H_{\mathrm{nl}}\Delta\gamma/2)\boldsymbol{\alpha}_n}{1 + H_{\mathrm{nl}}\Delta\gamma/2}, \tag{76}$$

where as follows by definitions (53) and (39), the normal at time t_{n+1} is given by

$$\mathbf{n}_{n+1} = \frac{\mathbf{X}^s_{n+1}}{X_{0,n+1}}. \tag{77}$$

Moreover, we note that the value of $\Delta\gamma$ in (76) can be obtained directly from definition (44)

$$\Delta\gamma = \begin{cases} \dfrac{\sigma_{\mathrm{y},0}}{2G_1}\ln(X_{0,n+1}/X_{0,n}) & \text{if } H_{\mathrm{iso}} = 0, \\ \dfrac{\sigma_{\mathrm{y},0}}{H_{\mathrm{iso}}}(X^q_{0,n+1} - X^q_{0,n}) & \text{if } H_{\mathrm{iso}} \neq 0. \end{cases} \tag{78}$$

4.3. Solution algorithm

At every time step the exponential-based algorithm proceeds as follows:

(1) Suppose the step to be elastic and compute trial values following an elastic law

$$\mathbf{X}^{\mathrm{TR}}_{n+1} = \overline{\mathbb{G}}_{\mathrm{e}}\mathbf{X}_n, \tag{79}$$

where the operator $\overline{\mathbb{G}}_{\mathrm{e}}$ is given by (72). If the trial solution is admissible, i.e.

$$\|\mathbf{X}^{s,\mathrm{TR}}_{n+1}\| \leqslant (X^{\mathrm{TR}}_{0,n+1})^2 \tag{80}$$

then the history variables at the time step t_{n+1} are taken as the trial ones just calculated.

(2) If the trial solution is not admissible, i.e. Eq. (80) is violated, then the step is plastic or elastoplastic. Being $\dot{\mathbf{e}}$ constant in each time sub interval, the step can be divided into two parts: an elastic deformation followed by a plastic one. We represent with a scalar $\alpha \in [0,1)$ the elastic time proportion of the step, which with simple geometrical considerations turns out to be

$$\alpha = \frac{\sqrt{C^2 - DM} - C}{D}, \tag{81}$$

where

$$\begin{cases} C = \dfrac{2GX_{0,n}}{\sigma_{\mathrm{y},n}}(\mathbf{X}^s_n : \Delta\mathbf{e}), \\ D = \left(\dfrac{2GX_{0,n}\|\Delta\mathbf{e}\|}{\sigma_{\mathrm{y},n}}\right)^2, \\ M = \|\mathbf{X}^s_n\|^2 - (X^{\mathrm{TR}}_{0,n+1})^2. \end{cases} \tag{82}$$

Computed α, $\mathbf{X}_{n+1}$ is updated in two steps.

- Calculate a new $\mathbf{X}^{\mathrm{e}}_{n+1}$ following an elastic law along an $\alpha\Delta t$ interval

$$\mathbf{X}^{\mathrm{e}}_{n+1} = \overline{\mathbb{G}}_{\mathrm{e}}[\alpha\Delta t]\mathbf{X}_n. \tag{83}$$

- Calculate $\mathbf{X}_{n+1}$ evolving from the new initial data $\mathbf{X}^{\mathrm{e}}_{n+1}$ following a plastic law along the remaining part of the interval of amplitude $(1-\alpha)\Delta t$

$$\mathbf{X}_{n+1} = \overline{\mathbb{G}}_{\mathrm{p}}[(1-\alpha)\Delta t]\mathbf{X}^{\mathrm{e}}_{n+1}. \tag{84}$$

Observe that in such a framework purely plastic steps are simply those where the time proportion of the elastic phase α is zero.

(3) Update the yield surface radius

$$\sigma_{\mathrm{y},n+1} = \sigma_{\mathrm{y}}(X_{0,n+1}) = \sigma_{\mathrm{y},0}(X_{0,n+1})^q, \tag{85}$$

$$q = \frac{H_{\mathrm{iso}}}{2G_1}, \tag{86}$$

which is easily obtained combining (35) and (44).

(4) Update the backstress $\boldsymbol{\alpha}$ as follows from (76)

$$\boldsymbol{\alpha}_{n+1} = \frac{H_{\mathrm{kin}}\Delta\gamma(\mathbf{n}_{n+1}+\mathbf{n}_n)/2 + (1 - H_{\mathrm{nl}}\Delta\gamma/2)\boldsymbol{\alpha}_n}{1 + H_{\mathrm{nl}}\Delta\gamma/2}, \tag{87}$$

where $\mathbf{n}_{n+1}$ and $\Delta\gamma$ can be calculated from (77) and (78) respectively. Note that, due to (35), in the case $H_{\mathrm{iso}} \neq 0$ the scalar $\Delta\gamma$ can be simply computed as

$$\Delta\gamma = \frac{\sigma_{\mathrm{y},n+1} - \sigma_{\mathrm{y},n}}{H_{\mathrm{iso}}}, \tag{88}$$

where $\sigma_{\mathrm{y},n+1}$ has been already updated in (85).

The updating procedure illustrated by steps (1)–(4) is represented in Fig. 1.

Remark 4.2. The relative stress can be calculated whenever needed as

$$\boldsymbol{\Sigma} = \frac{\mathbf{X}^s}{X_0}\sigma_{\mathrm{y}}, \tag{89}$$

which is immediately obtained from the definition of $\mathbf{X}$.

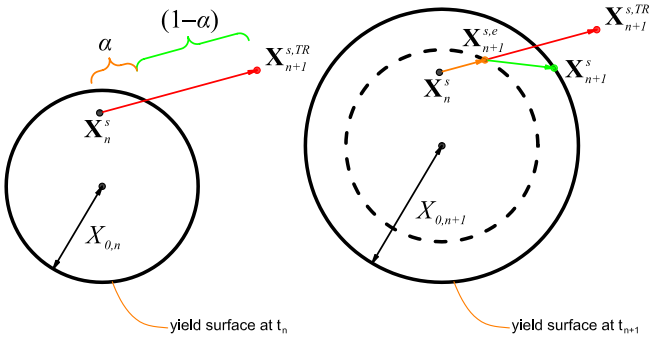

Fig. 1. Exponential-based scheme update procedure in the generalized relative stress space during a mixed elastoplastic step.

Remark 4.3. The variable X_0 is a local auxiliary variable and not an history variable. In other words, introducing an appropriate scaling of the couple $\mathbf{X}$, the variable X_0 does not need to be updated at every time step. See Remark 3 in [1] for a deeper explanation of these algorithmical issues.

Remark 4.4. The scalar α in the ESC^{2}nl scheme is not to be confused with the α parameter of the midpoint method presented in this same contribution. The authors preferred to avoid renaming variables which already appear in the existing literature.

4.4. Elastoplastic consistent tangent operator

The algorithmically consistent tangent operator can be obtained properly linearizing the ESC^{2}nl procedure. In the present paragraph all the history variables are to be intended evaluated at the end of the time step t_{n+1}; therefore all subscripts will be omitted for the sake of compactness.

For the total stress, from (23) and (5) it immediately follows

$$\mathbb{D}_{\text{disc}} = \frac{\partial \boldsymbol{\sigma}}{\partial \boldsymbol{\varepsilon}} = \left[\frac{\partial \boldsymbol{\Sigma}}{\partial \mathbf{e}} + \frac{\partial \boldsymbol{\alpha}}{\partial \mathbf{e}}\right] : \mathbb{I}_{\text{dev}} + K(\mathbf{I}\otimes\mathbf{I}). \tag{90}$$

As shown in [1,2], a few calculations give

$$\frac{\partial \boldsymbol{\Sigma}}{\partial \mathbf{e}} = \frac{\sigma_y}{X_0}\left(\frac{\partial \mathbf{X}^s}{\partial \mathbf{e}} - \frac{1-q}{X_0}\mathbf{X}^s \otimes \frac{\partial X_0}{\partial \mathbf{e}}\right), \tag{91}$$

while a direct derivation of the update procedure (87) gives $\frac{\partial \boldsymbol{\alpha}}{\partial \mathbf{e}}$, which is shown in Appendix A.

For the elastic phase we immediately have

$$\frac{\partial \mathbf{X}^s}{\partial \mathbf{e}} = 2GX_0\mathbb{I}, \tag{92}$$

$$\frac{\partial X_0}{\partial \mathbf{e}} = \mathbf{0}, \tag{93}$$

while in the plastic phase the result is far more complicated and can be found in Appendix A.

4.5. Brief review of the exponential-based algorithm numerical properties

The presented ESC^{2}nl method satisfies the following algorithmical properties:

Yield consistency. As shown in (60), in the framework of formulation (56) the yield condition becomes

$$\|\mathbf{X}^s\|^2 = X_0^2 \tag{94}$$

at the end of all plastic steps.

Applying the same proof as in [1], it can be immediately shown that such condition is fullfilled by the ESC^{2}nl scheme here presented.

Second-order accuracy. Following standard calculations, namely a Taylor expansion in time, it can be proved that the truncation error of the ESC^{2}nl method is of order $(\Delta t)^2$ during purely plastic steps, where Δt is the time step size. Therefore the scheme is second-order accurate, which guarantees a very reduced error at small time steps.

Exactness in case of no hardening. If $H_{\text{iso}} = H_{\text{nl}} = H_{\text{kin}} = 0$, provided $\mathbf{e}(t)$ is piecewise constant, the matrix in (56) is constant during each time step. As a consequence, the evolution problem (56) is integrated exactly by the exponential-based method presented. Therefore, whenever $H_{\text{iso}} = H_{\text{nl}} = H_{\text{kin}} = 0$, no error is introduced by the scheme in strain driven loading histories characterized by a strain tensor evolving piecewise linearly in time. Nevertheless, this property does not imply exactness in the general mixed stress–strain driven case, as discussed in [2].

The reader is referred to [2] for a deeper discussion on the algorithmical properties of exponential-based methods in the case of von-Mises plasticity with linear isotropic and kinematic hardening.

Remark 4.5. Stability of the method is, from the theoretical viewpoint, still to be addressed. In [2], a stability analysis is developed for two exponential-based methods applied to the von-Mises elastoplastic model with linear hardening.

5. Numerical tests

In this section we present an extensive set of numerical examples by means of which we compare the MPTnl and ESC^{2}nl methods performances. For brevity's sake, throughout this section we adopt the following labels:

- BEnl Backward Euler method ([4] and Section 3.3.2).
- MPTnl Midpoint method (Section 3.1).
- ESC^{2}nl Exponential-based method (Section 4.1).

The numerical tests are divided in three parts. In the first one, we consider mixed stress–strain loading histories for a material point. The object of this test is to study the precision granted by the method with respect to the computation of the stress and of the strain in a typical loading history. In the second part, we show a set of iso-error maps in order to investigate the algorithm precision using different time discretizations. Finally, we present a classical boundary value problem, which we study to analyze the algorithm reliability on a practical engineering problem.

As a result of the above numerical tests we carry out a detailed comparison of the presented methods in terms of performances. The pointwise tests and the iso-error maps are performed with the CE-Driver [5], while the boundary value problem is solved using FEAP [22]. Each test will be described in detail at the beginning of the pertinent section.

In the analysis we consider two sets of material constants

- Material 1 (see [23])

$$E = 2\times10^5\,\text{MPa},\quad \nu = 0.3,\quad \sigma_{y,0} = 2\times10^2\,\text{MPa},$$
$$H_{\text{iso}} = 0\,\text{MPa},\quad H_{\text{kin}} = 2\times10^4\,\text{MPa},\quad H_{\text{nl}} = 50\,\text{MPa},$$
$$\overline{H}_{\text{iso}} = H_{\text{iso}}/E = 0,\quad \overline{H}_{\text{kin}} = H_{\text{kin}}/E = 10^{-1},\quad \overline{H}_{\text{nl}} = H_{\text{nl}}/E = 2.5\times10^{-4}.$$

- Material 2 (see [23])

$E = 2 \times 10^5$ MPa, $\nu = 0.3$, $\sigma_{y,0} = 2 \times 10^2$ MPa,
$H_{iso} = 6 \times 10^3$ MPa, $H_{kin} = 2 \times 10^4$ MPa, $H_{nl} = 50$ MPa,
$\overline{H}_{iso} = H_{iso}/E = 3 \times 10^{-2}$, $\overline{H}_{kin} = H_{kin}/E = 10^{-1}$, $\overline{H}_{nl} = H_{nl}/E = 2.5 \times 10^{-4}$.

Finally, we recall that the Young Modulus E and the Poisson ratio ν uniquely determine the constants K and G as follows:

$$K = \frac{E}{3(1-2\nu)}, \quad G = \frac{E}{2(1+\nu)}.$$

5.1. Mixed stress–strain loading histories

We consider three biaxial non-proportional stress–strain histories. The loading histories are obtained assuming to control two strain components and requiring that all the stress components not corresponding to the two controlled strains are identically equal to zero. In particular, in the three biaxial problems we control the following strain components:

Problem 1: ε_{11} ε_{12},
Problem 2: ε_{11} ε_{22},
Problem 3: ε_{11} ε_{12}.

It is noted that Problem 1 and Problem 3 are set controlling the same strain components, which evolve according to different loading histories as reported in Fig. 2. In particular, the controlled strain components are increased up to a maximum value of $5\varepsilon_{y,mono}$ where the quantity

$$\varepsilon_{y,mono} = \sqrt{\frac{3}{2}}\frac{\sigma_{y,0}}{E} \tag{95}$$

represents the first yielding strain value in a uniaxial strain loading history.

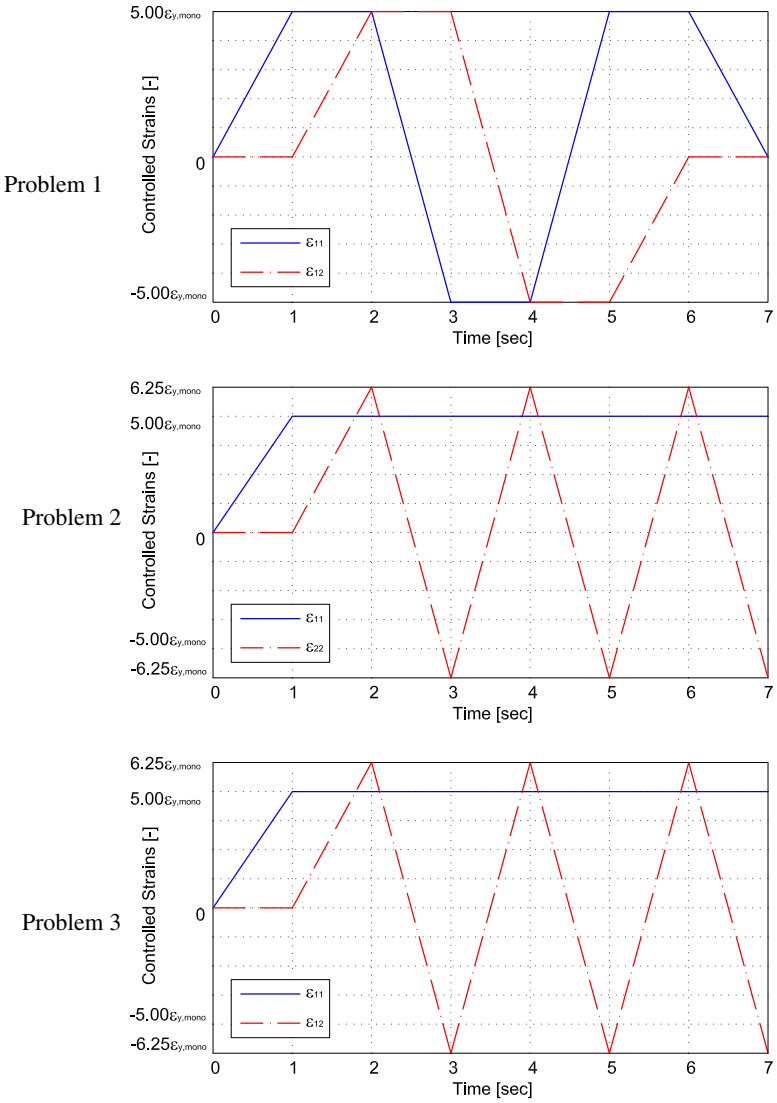

Fig. 2. Pointwise stress–strain tests. Mixed stress–strain load histories for Problems 1–3.

5.1.1. Instantaneous error

The scope of this test is to evaluate the precision granted by an algorithm in the stress–strain computation for the solution of a loading history. This task is achieved comparing the stress and strain output obtained using prescribed time discretizations with a reference solution.

Lacking the analytical solution of the problems under investigation, we compute the reference stress and strain response using the BEnl scheme with a very fine time discretization, corresponding to 100,000 steps per second ($\Delta t = 0.00001$ s). Such a solution is compared with solutions corresponding respectively to 10, 20 and 40 steps per second ($\Delta t = 0.1$ s, 0.05 s, 0.025 s) and computed with the BEnl, MPTnl and ESC^{2}nl algorithms respectively.

The error is evaluated separately for the stress and the strain and for each time discretization, in order to appreciate the dependence of the error on the time step size Δt. To this end we introduce the following relative norms

$$E_n^{\boldsymbol{\sigma}} = \frac{\|\boldsymbol{\sigma}_n - \boldsymbol{\sigma}_n^{\mathrm{ex}}\|}{\sigma_{\mathrm{y},n}} \qquad E_n^{\boldsymbol{\varepsilon}} = 2G\frac{\|\boldsymbol{\varepsilon}_n - \boldsymbol{\varepsilon}_n^{\mathrm{ex}}\|}{\sigma_{\mathrm{y},n}}, \tag{96}$$

where $\|\bullet\|$ indicates the usual Euclidean norm and $\sigma_{\mathrm{y},n}$ is the yield surface radius at time t_n. In Eq. (96), $\boldsymbol{\sigma}_n^{\mathrm{ex}}$ and $\boldsymbol{\varepsilon}_n^{\mathrm{ex}}$ are respectively the stress and the strain reference solution at time t_n. The quantities $\boldsymbol{\sigma}_n$ and $\boldsymbol{\varepsilon}_n$ represent the stress and strain tensors respectively, computed adopting the prescribed time discretizations ($\Delta t = 0.1$ s, 0.05 s, 0.025 s). Fig. 3 reports stress and strain relative errors (96) using Material 1 for the first loading history and for the three different time discretizations indicated above, using all the three compared methods. Fig. 4 reports the same quantities using Material 2 for the second loading history; for

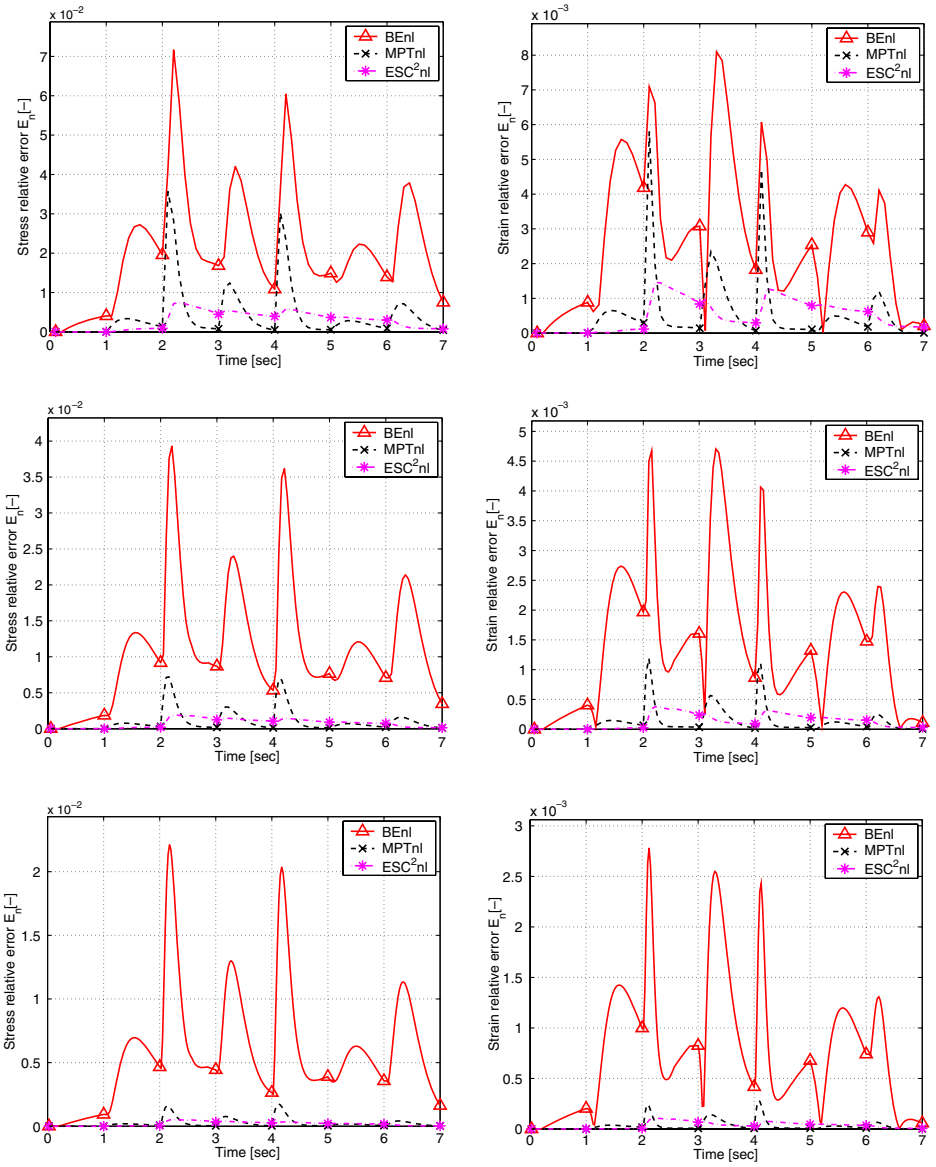

Fig. 3. Pointwise stress–strain tests: Problem 1 with Material 1. Stress and strain error for $\Delta t = 0.1$ s, $\Delta t = 0.05$ s, $\Delta t = 0.025$ s.

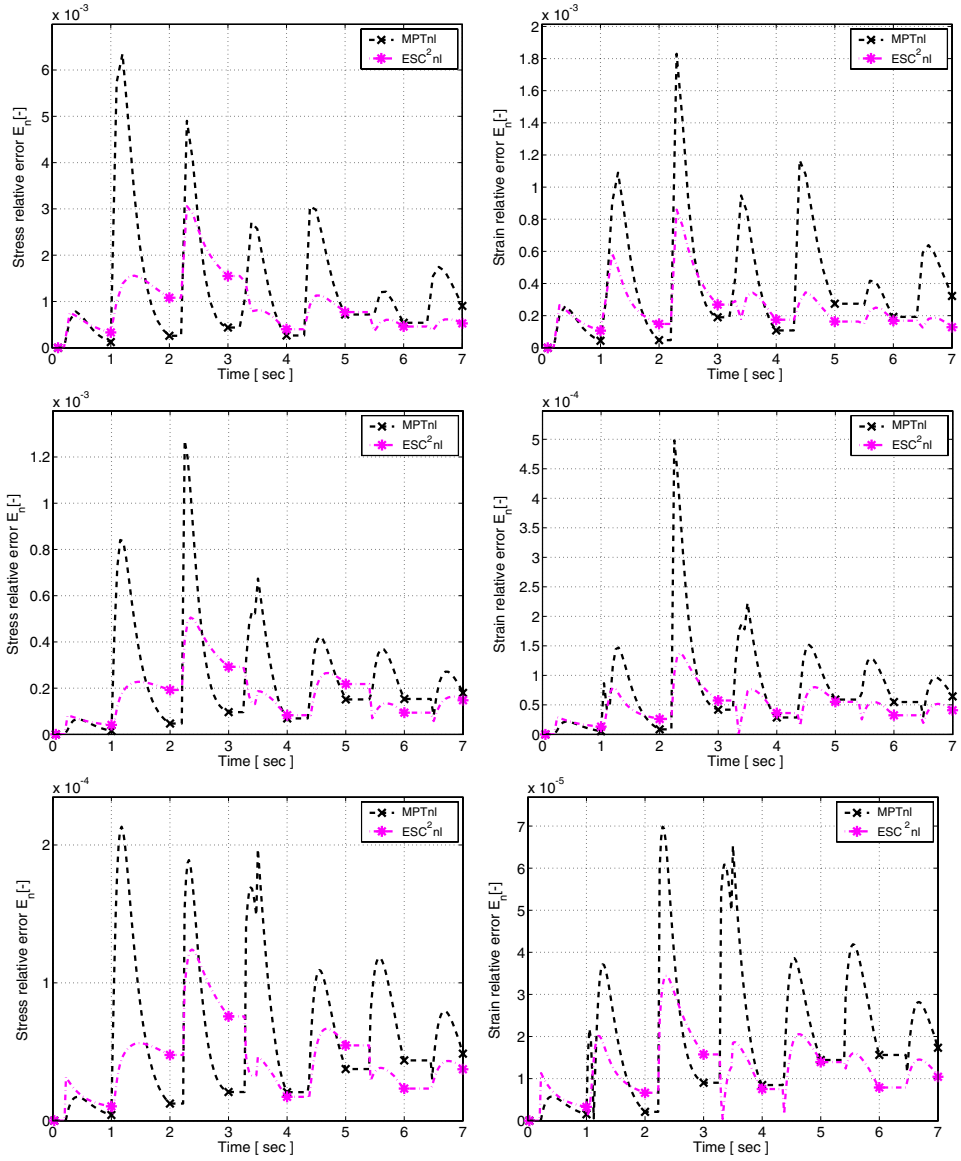

Fig. 4. Pointwise stress–strain tests: Problem 2 with Material 2. Stress and strain error for $\Delta t = 0.1$ s, $\Delta t = 0.05$ s, $\Delta t = 0.025$ s.

brevity's reasons Fig. 4 reports data only for the quadratic methods MPTnl and ESC^{2}nl. We choose to present this limited number of error graphs since they are well representative of the comparative behavior enlightened during the full set of tests. It is evident from the presented error plots that

- The BEnl method is linearly accurate, that is the error is proportional to the step size Δt, while both the MPTnl and ESC^{2}nl are quadratically accurate, that is the error is proportional to the square of Δt.
- The performance of the MPTnl and ESC^{2}nl methods are globally comparable. As the loading history evolves the exponential-based method seems to produce lower error levels than the midpoint algorithm when there is a direction change in the driving input. Inspecting Figs. 3 and 4, it is noted that the dashed line peaks on the error plots are usually higher than the dash-dot line peaks. On the other hand, in most cases it is observed that the MPTnl algorithm error levels decrease more rapidly after the change of direction peaks than in the case of the ESC^{2}nl method.
- The two second-order accurate methods ESC^{2}nl and MPTnl perform decisively better than the linearly accurate BEnl, for all the considered stress–strain loading histories.

5.1.2. Total error

In order to further investigate rate of convergence of the tested method, we also introduce the average *total error* as the scaled ℓ^1 norm in time of the absolute error:

$$E_T^{\boldsymbol{\sigma}} = \frac{\Delta t}{T} \sum_{n=1}^{N} \frac{\|\boldsymbol{\sigma}_n - \boldsymbol{\sigma}_n^{\mathrm{ex}}\|}{\sigma_{\mathrm{y},n}} \qquad E_T^{\boldsymbol{\varepsilon}} = 2G \frac{\Delta t}{T} \sum_{n=1}^{N} \frac{\|\boldsymbol{\varepsilon}_n - \boldsymbol{\varepsilon}_n^{\mathrm{ex}}\|}{\sigma_{\mathrm{y},n}}. \quad (97)$$

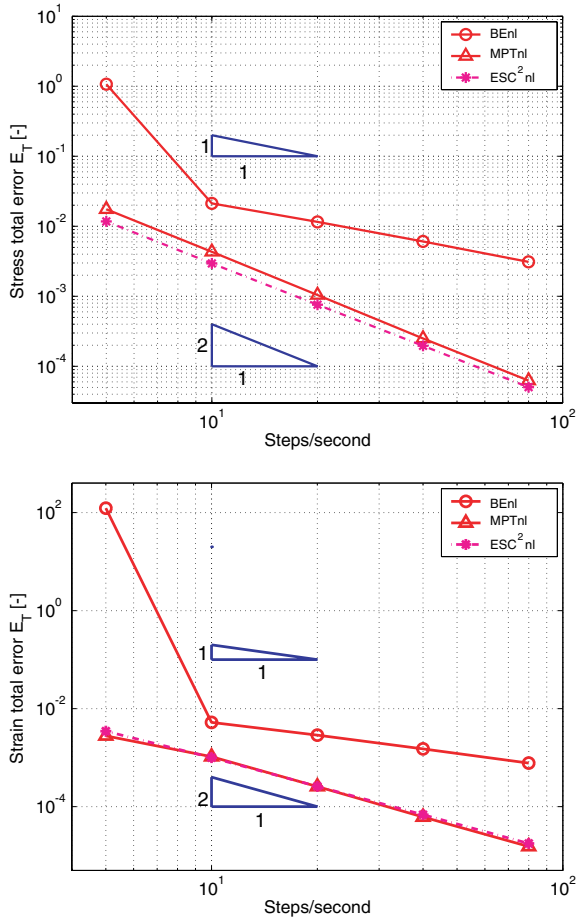

Fig. 5. Pointwise stress–strain tests. Problem 1 with Material 1. Stress and strain total error versus number of steps per second.

In Fig. 5 we plot the total error versus the number of time steps in logarithmic scale for the three methods BEnl, MPTnl and ESC^{2}nl for Problem 1 with Material 1. The quadratic convergence of the MPTnl and ESC^{2}nl methods, with respect to the linear one of the BEnl algorithm is still evident. Moreover, the quadratic methods show significantly lower error levels with respect to the ones granted by the linear method.

5.2. Iso-error maps

Iso-error maps are commonly adopted in the literature [12,15,16,18] as a systematic tool to test the precision of plasticity integration algorithms. In particular, they render a clear evaluation of the integration algorithm precision when a large time discretization is adopted. Error maps are plotted as a result of particular mixed stress–strain loading histories which are piecewise linear in time.

Each loading history is set up by controlling for example the ε_{11} and ε_{22} strain components and requiring all the remaining stresses to be equal to zero. The evolution in time of the controlled quantities is piecewise linear and can be divided in two distinct phases defined as follows (see Table 1). Phase 1 consists of a purely elastic path and proceeds from the zero stress and strain state (State 0) to a specific state on the yield surface (State 1) given in terms of the yield strain components $\varepsilon_{11,y}$ and $\varepsilon_{22,y}$. Phase 2 is a purely plastic path which starts from State 1 and leads to a final state (State 2) given in terms of the strain increments $\Delta\varepsilon_{11}$ and $\Delta\varepsilon_{22}$.

In this analysis, we consider three different choices of State 1, corresponding to plane states of stress on the yield surface [18], labeled **A**, **B** and **C** respectively, represented in Fig. 6 and corresponding to uniaxial, biaxial and pure shear states. Each State 1 is expressed in Table 2 in terms of the quantity $\varepsilon_{y,mono}$ defined in (95) according to

$$\varepsilon_{11} = \varepsilon_{11,y},$$
$$\varepsilon_{22} = \varepsilon_{22,y}.$$

For each choice of State 1, we then consider a State 2 defined as

$$\varepsilon_{11} = \varepsilon_{11,y} + \Delta\varepsilon_{11},$$
$$\varepsilon_{22} = \varepsilon_{22,y} + \Delta\varepsilon_{22}.$$

Table 1
Benchmark mixed stress–strain history for iso-error maps computation

	Time (s)	ε_{11}	ε_{22}	σ_{33}	σ_{12}	σ_{13}	σ_{23}
State 0	$t=0$	0	0	0	0	0	0
State 1	$t=1$	$\varepsilon_{11,y}$	$\varepsilon_{22,y}$	0	0	0	0
State 2	$t=2$	$\varepsilon_{y,11}+\Delta\varepsilon_{11}$	$\varepsilon_{y,22}+\Delta\varepsilon_{22}$	0	0	0	0

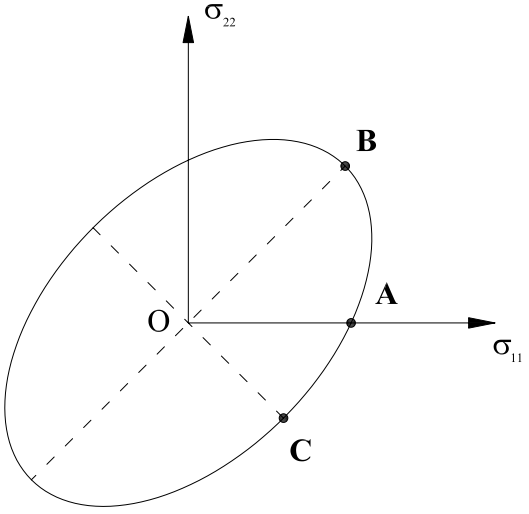

Fig. 6. Plane stress von-Mises yield surface representation in principal stresses plane. State 1 choices for iso-error maps plots.

Table 2
Iso-error maps

	$\varepsilon_{11,y}$	$\varepsilon_{22,y}$	σ_{33}	σ_{12}	σ_{13}	σ_{23}
State 1-A	$\varepsilon_{y,mono}$	$-\nu\varepsilon_{y,mono}$	0	0	0	0
State 1-B	$(1-\nu)\varepsilon_{y,mono}$	$\varepsilon_{y,mono}$	0	0	0	0
State 1-C	$\frac{(1+\nu)}{3}\varepsilon_{y,mono}$	$-\frac{(1+\nu)}{3}\varepsilon_{y,mono}$	0	0	0	0

Choices for the State 1 point on the yield surface.

We solve a total of 60×60 mixed stress–strain histories for each State 1, corresponding to the following sets of normalized strain increments (see Figs. 7–9)

$$\frac{\Delta\varepsilon_{11}}{\varepsilon_{11,y}} = 0.0, 0.1, 0.2, \ldots, 6.0,$$

$$\frac{\Delta\varepsilon_{22}}{\varepsilon_{22,y}} = 0.0, 0.1, 0.2, \ldots, 6.0.$$

This subdivision leads to a total of 3600 computed mixed stress–strain loading histories and to an equal number of calculated relative error values. According to [21,18], as an error measure, we adopt the following expression

$$E^{\sigma}_{\mathrm{iso}} = \frac{\|\boldsymbol{\sigma} - \boldsymbol{\sigma}^{\mathrm{ex}}\|}{\|\boldsymbol{\sigma}^{\mathrm{ex}}\|}, \tag{98}$$

where $\boldsymbol{\sigma}$ is the final stress tensor, computed adopting a single time step discretization between State 1 and State 2, whereas $\boldsymbol{\sigma}^{\mathrm{ex}}$ corresponds to an "exact" solution adopting a very fine time step between State 1 and State 2. All the calculations refer to Material 2 [18].

The total error range is subdivided in ten equally spaced levels according to which the iso-curves are drawn in Figs. 7–9. Each iso-curve is indicated by a proper error label while the thick continuous line represents the cou-

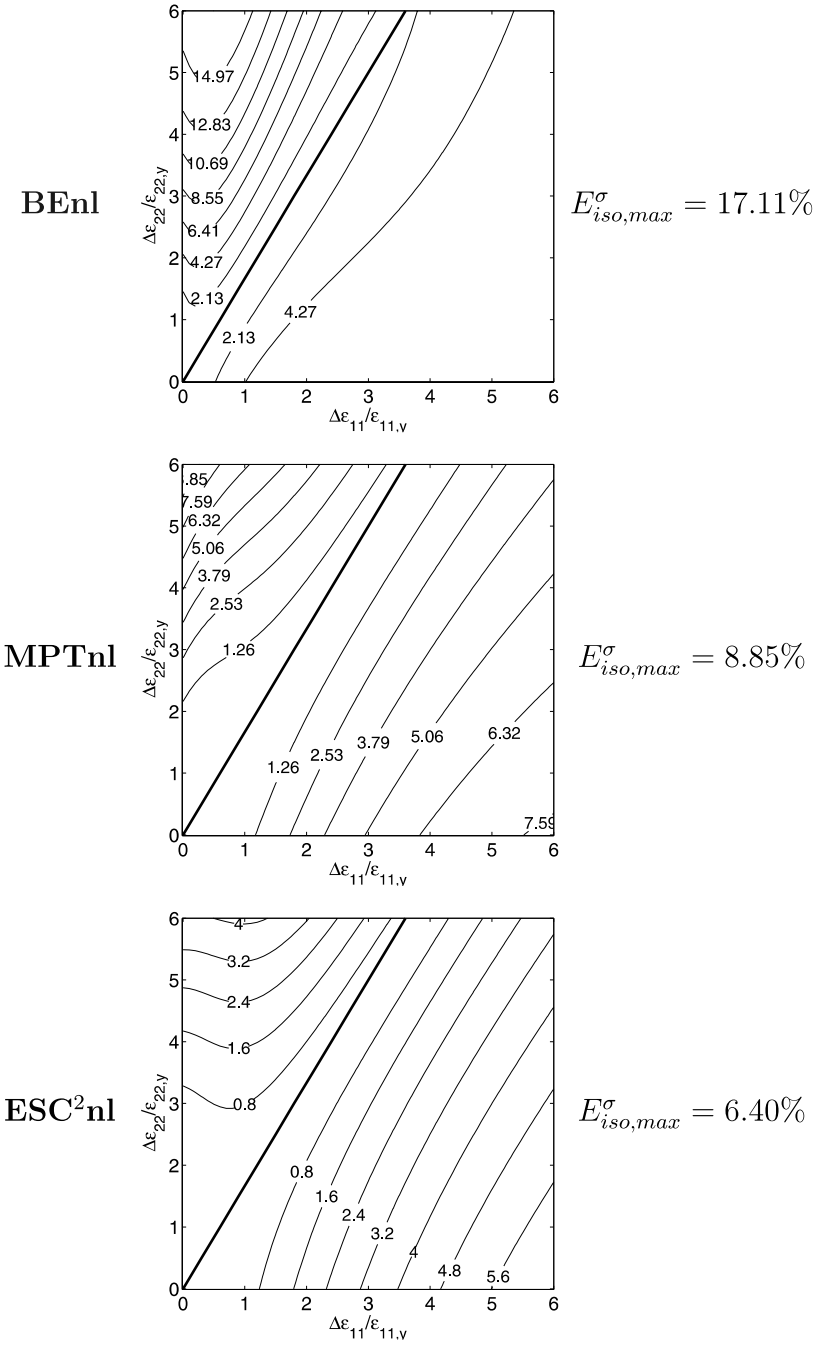

Fig. 7. Comparison between backward Euler (BEnl), midpoint (MPTnl) and the new exponential-based scheme (ESC^{2}nl). Iso-error maps for Material 2. Yield surface State 1-A and indication of the maximum stress error level.

ples of strain increments values corresponding to proportional loading histories starting from State 1. For the sake of completeness, aside from each map we also report the maximum error value computed on the grid adopted for the computation of the iso-error map. Observing Figs. 7–9 we can derive the following conclusions

- The ESC^{2}nl scheme shows better performances than both the BEnl and MPTnl algorithms for every considered starting yield State 1-A, 1-B and 1-C. Even for "large" strain increments the new exponential-based procedure reveals low levels of error compared with the other two methods in all the examined cases.
- In general the BEnl scheme presents lower error levels for large strain increments than the MPTnl method. This result is in agreement with the general observation that lower order methods perform better than higher order ones for large time steps.
- None of the algorithms presents a zero error level along proportional loading paths (thick black lines, Figs. 7–9). This is due to the fact that we have taken into account a

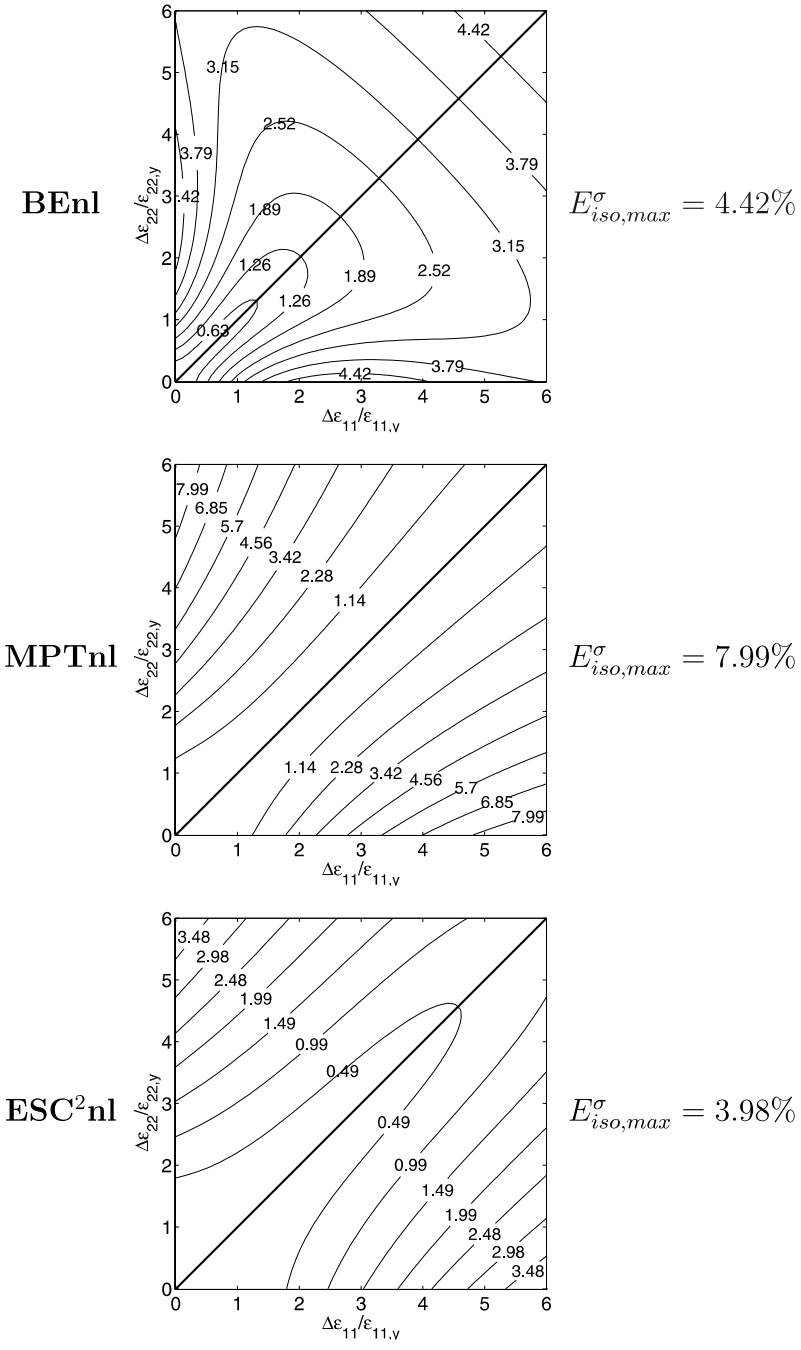

Fig. 8. Comparison between backward Euler (BEnl), midpoint (MPTnl) and the new exponential-based scheme (ESC^{2}nl). Iso-error maps for Material 2. Yield surface State 1-B and indication of the maximum stress error level.

nonlinear kinematic hardening mechanism. Again in the vicinity of these lines the exponential-based method seems to be more precise than the other schemes.

5.3. An initial boundary value problem

We consider a boundary value problem regarding the elongation of a rectangular strip with a circular hole in the centre, assuming plane strain regime [18]. The strip possesses three planes of symmetry mutually orthogonal. Then, as can be seen in Fig. 10(a), only a quarter of it is sufficient to define its geometry. The lengths referred to Fig. 10(a) are

$$B = 100\ \text{mm}, \quad H = 180\ \text{mm}, \quad B_0 = 50\ \text{mm},$$

while the thickness is 10 mm.

Initially the strip results undeformed and unstressed. The problem loading history results symmetric with respect to the three symmetry planes of the strip, hence we can refer to a single quarter of the domain and define the following equivalent problem. The loading history is composed of a first phase (1 s), in which, the strip is stretched assigning a top side vertical displacement $\delta_{\max}$ and a second phase (1 s) in which the imposed displacement is set back to 0 mm. We set $\delta_{\max} = 1$ mm. We assume to block

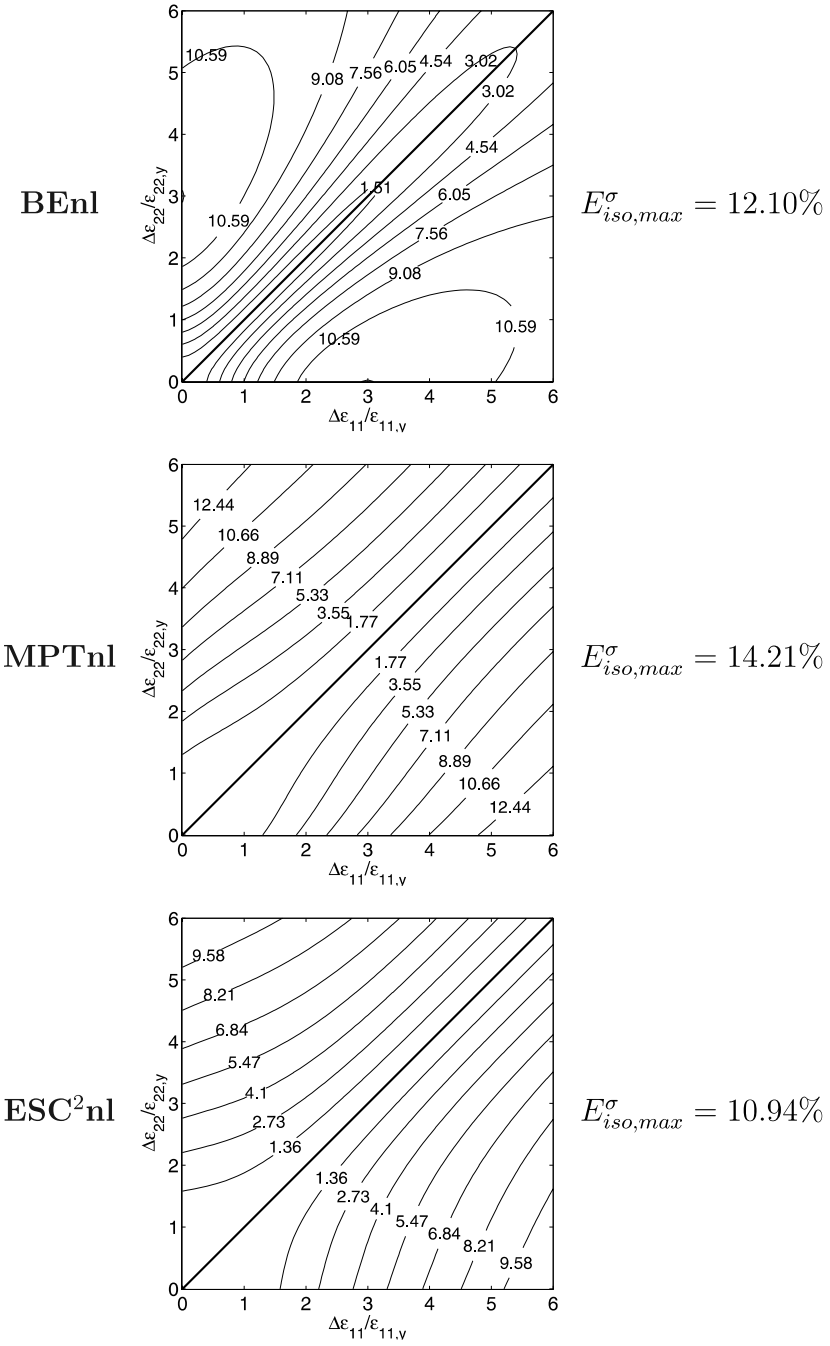

Fig. 9. Comparison between backward Euler (BEnl), midpoint (MPTnl) and the new exponential-based scheme (ESC^{2}nl). Iso-error maps for Material 2. Yield surface State 1-C and indication of the maximum stress error level.

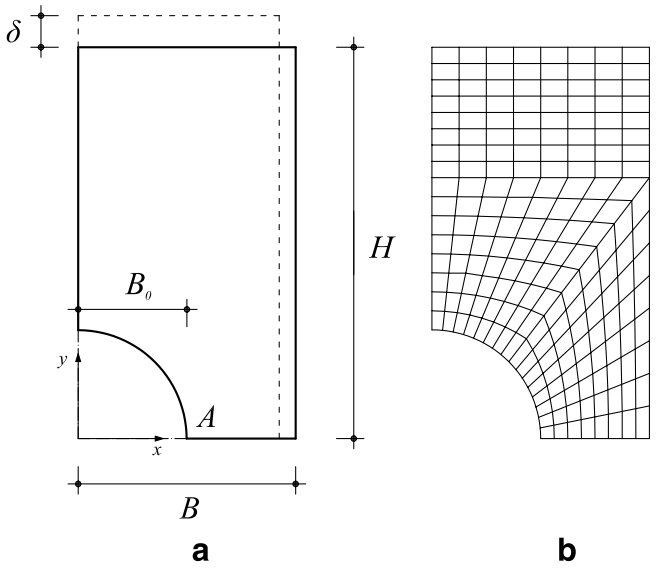

Fig. 10. Boundary value problem. (a) Strip with circular hole. (b) Plane projection of the adopted mesh.

the horizontal displacement on the left side and to block the vertical displacement on the bottom side of the strip. The remaining boundary sides are stress free. In the analysis we consider Material 2 as done for the iso-error map tests.

We solve the boundary value problem using the finite element code FEAP [22], in which the considered integration methods are implemented. The mesh is composed of N_{el} finite elements (displacement-based four-node SOLID2D elements adopting a four point Gauss quadrature rule [22]). The following results refer to a mesh with $N_{\text{el}} = 192$ as can be observed in Fig. 10(b).

The comparison between the methods is carried out by evaluating the following L^2 norm error on stress and strain

$$\widetilde{E}^{\boldsymbol{\sigma}} = \sqrt{\frac{\int_{\Omega} \|\boldsymbol{\sigma}_n - \boldsymbol{\sigma}_n^{\text{ex}}\|^2}{\int_{\Omega} \|\boldsymbol{\sigma}_n^{\text{ex}}\|^2}}, \tag{99}$$

$$\widetilde{E}^{\boldsymbol{\varepsilon}} = \sqrt{\frac{\int_{\Omega} \|\boldsymbol{\varepsilon}_n - \boldsymbol{\varepsilon}_n^{\text{ex}}\|^2}{\int_{\Omega} \|\boldsymbol{\varepsilon}_n^{\text{ex}}\|^2}}. \tag{100}$$

The quantities $\boldsymbol{\sigma}_n$ and $\boldsymbol{\varepsilon}_n$ are, respectively, the stress and strain tensors calculated via the three integration schemes adopting a prescribed time step Δt, while $\boldsymbol{\sigma}_n^{\text{ex}}$ and $\boldsymbol{\varepsilon}_n^{\text{ex}}$ are the corresponding reference solutions evaluated with the reference BEnl scheme using a time step $\Delta t = 0.00001$ s. In the following tests we have chosen three different time steps sizes, respectively $\Delta t_1 = 0.05$ s, $\Delta t_2 = 0.025$ s, $\Delta t_3 = 0.0125$ and we have evaluated the norms (99) and (100) at four different instants of the loading history with the three discretizations described above. The results are summarized in Table 3.

Table 3
Boundary value problem

$\widetilde{E}$	Δt	BEnl	MPTnl	ESC^{2}nl
t = 0.5				
$\widetilde{E}^{\boldsymbol{\sigma}}$	Δt_1	4.41×10^{-3}	2.27×10^{-4}	3.95×10^{-4}
	Δt_2	2.27×10^{-3}	6.11×10^{-5}	1.04×10^{-4}
	Δt_3	1.15×10^{-3}	1.61×10^{-5}	2.61×10^{-5}
$\widetilde{E}^{\boldsymbol{\varepsilon}}$	Δt_1	3.72×10^{-3}	5.83×10^{-4}	6.44×10^{-4}
	Δt_2	1.91×10^{-3}	1.52×10^{-4}	1.62×10^{-4}
	Δt_3	9.65×10^{-4}	3.94×10^{-5}	4.15×10^{-5}
t = 1.0				
$\widetilde{E}^{\boldsymbol{\sigma}}$	Δt_1	3.33×10^{-3}	6.87×10^{-5}	1.86×10^{-4}
	Δt_2	1.69×10^{-3}	1.84×10^{-5}	4.95×10^{-5}
	Δt_3	8.48×10^{-4}	4.92×10^{-6}	1.25×10^{-5}
$\widetilde{E}^{\boldsymbol{\varepsilon}}$	Δt_1	2.74×10^{-3}	1.97×10^{-4}	2.52×10^{-4}
	Δt_2	1.40×10^{-3}	5.17×10^{-5}	6.34×10^{-5}
	Δt_3	7.05×10^{-4}	1.32×10^{-5}	1.63×10^{-5}
t = 1.5				
$\widetilde{E}^{\boldsymbol{\sigma}}$	Δt_1	1.48×10^{-2}	1.62×10^{-3}	7.50×10^{-4}
	Δt_2	7.98×10^{-3}	4.42×10^{-4}	1.86×10^{-4}
	Δt_3	4.17×10^{-3}	1.10×10^{-4}	4.51×10^{-5}
$\widetilde{E}^{\boldsymbol{\varepsilon}}$	Δt_1	3.13×10^{-3}	2.21×10^{-4}	3.04×10^{-4}
	Δt_2	1.54×10^{-3}	6.06×10^{-5}	7.08×10^{-5}
	Δt_3	7.63×10^{-4}	1.40×10^{-5}	1.92×10^{-5}
t = 2.0				
$\widetilde{E}^{\boldsymbol{\sigma}}$	Δt_1	5.05×10^{-3}	2.22×10^{-4}	2.14×10^{-4}
	Δt_2	2.57×10^{-3}	5.71×10^{-5}	5.15×10^{-5}
	Δt_3	1.29×10^{-3}	1.48×10^{-5}	1.24×10^{-5}
$\widetilde{E}^{\boldsymbol{\varepsilon}}$	Δt_1	8.08×10^{-3}	4.94×10^{-4}	9.74×10^{-4}
	Δt_2	4.16×10^{-3}	1.13×10^{-4}	2.30×10^{-4}
	Δt_3	2.10×10^{-3}	3.19×10^{-5}	6.45×10^{-5}

Stress and strain L^2 norm errors with Material 2 at $t = 0.5$, $t = 1.0$, $t = 1.5$, $t = 2.0$.

As expected, by inspecting Table 3, we observe that the BEnl shows first-order accuracy while the MPTnl and ESC^{2}nl are second-order accurate schemes. The quadratically accurate MPTnl and ESC^{2}nl algorithms result comparable in terms of precision.

6. Conclusions

The present work focuses on a von-Mises plasticity model with linear isotropic and kinematic hardening and nonlinear kinematic hardening, in the realm of small deformations. The paper presents two second-order methods for the aforementioned model.

The first scheme, labeled MPTnl, is an application of the generalized midpoint integration algorithm of Ortiz and Popov [15], here for the first time implemented and tested in the case of nonlinear kinematic hardening. The second scheme, referred as ESC^{2}nl, is based on a model quasi-linear reformulation combined with an exponential-based time integration method. This scheme belong to the class of exponential-based integration algorithms for von-Mises plasticity with linear hardening studied in [2].

After presenting the MPTnl and ESC^{2}nl methods, extensive numerical tests are carried out in order to compare the performances of the two schemes. In particular, the numerical tests comprise pointwise mixed stress–strain loading histories, iso-error maps and an initial boundary value problem on a perforated strip.

From the numerical tests, the MPTnl and ESC^{2}nl schemes seem to behave similarly. In particular, both methods are second-order accurate and result exact in case of no hardening. The higher peaks shown by the midpoint method in the pointwise loading histories error plots reveal higher precision of the exponential-based scheme whenever there is a crossing of the yield surface. Beyond this difference, the iso-error maps and the initial boundary value problem tests, suggest that the precision in stress and strain computation of the two schemes are comparable both for small and large time step size.

Appendix A

We present here the elastoplastic consistent tangent operator consistent with the ESC^{2}nl for an elastoplastic step. Recalling the developments carried out in Section 4.1, the present algorithmic tangent operator computation relies on the evaluation of the fourth-order tensors $\partial\mathbf{X}/\partial\mathbf{e}$ and $\partial\boldsymbol{\alpha}/\partial\mathbf{e}$. To make notation more clear, the subscripts of all history variables evaluated at the end of the time interval t_{n+1} are omitted for brevity. Quantities evaluated either at t_n or at $t_{n+\alpha}$ are specified by the relative subscript. Following the algorithm ESC^{2}nl of Section 4.1, for a general mixed elastoplastic step one has

$$\mathbf{X}^s = \mathbf{X}_n^{s,\mathrm{e}} + \frac{a-1}{\|\Delta\widehat{\boldsymbol{\Psi}}\|^2}(\Delta\widehat{\boldsymbol{\Psi}} : \mathbf{X}_n^{s,\mathrm{e}})\Delta\widehat{\boldsymbol{\Psi}} + b\frac{X_{0,n}}{\|\Delta\widehat{\boldsymbol{\Psi}}\|}\Delta\widehat{\boldsymbol{\Psi}}, \tag{A.1}$$

where

$$\mathbf{X}_n^{s,\mathrm{e}} = \mathbf{X}_n^s + \alpha\frac{2G}{\sigma_{\mathrm{y},n}}X_{0,n}\Delta\mathbf{e}, \tag{A.2}$$

$$a = \cosh\left[(1-\alpha)\frac{2G}{\bar{\sigma}_{\mathrm{y}}}\|\Delta\widehat{\boldsymbol{\Psi}}\|\right], \tag{A.3}$$

$$b = \sinh\left[(1-\alpha)\frac{2G}{\bar{\sigma}_{\mathrm{y}}}\|\Delta\widehat{\boldsymbol{\Psi}}\|\right], \tag{A.4}$$

$$\Delta\widehat{\boldsymbol{\Psi}} = \Delta\overline{\boldsymbol{\Psi}}_0 + (1-\alpha)\Delta\overline{\boldsymbol{\Psi}}_1. \tag{A.5}$$

Above, $\mathbf{X}_n^{s,\mathrm{e}}$ represents the value of the second-order tensor $\mathbf{X}^s$ updated at the end of the elastic part of the step. Moreover, $\Delta\widehat{\boldsymbol{\Psi}}$ is the scaled driving tensor, introduced to take into account that the plastic proportion of the step amounts to $(1-\alpha)\Delta t$.

The fourth-order tensor $\partial\mathbf{X}^s/\partial\mathbf{e}$ is obtained deriving expression (A.1). Without presenting all the calculations, it is found that

$$\frac{\partial\mathbf{X}^s}{\partial\mathbf{e}} = \mathbb{T}_1 + \mathbb{T}_2 + \mathbb{T}_3. \tag{A.6}$$

In order to describe the three addenda $\mathbb{T}_1$, $\mathbb{T}_2$ and $\mathbb{T}_3$, a set of preliminary derivatives is necessary.

Thus, we start introducing the second-order tensor $\boldsymbol{\upsilon} = \mathrm{d}\alpha/\mathrm{d}\Delta\mathbf{e}$

$$\begin{cases} \boldsymbol{\upsilon} = \phi_1\dfrac{\mathrm{d}C}{\mathrm{d}\Delta\mathbf{e}} + \phi_2\dfrac{\mathrm{d}D}{\mathrm{d}\Delta\mathbf{e}}, \\ \phi_1 = \dfrac{1}{D}\left(\dfrac{C}{\sqrt{C^2-DM}} - 1\right), \\ \phi_2 = -\dfrac{1}{D^2}\left(\dfrac{DM}{2\sqrt{C^2-DM}} + \sqrt{C^2-DM} - C\right), \\ \dfrac{\mathrm{d}C}{\mathrm{d}\Delta\mathbf{e}} = 2GX_{0,n}\mathbf{X}_n^s, \\ \dfrac{\mathrm{d}D}{\mathrm{d}\Delta\mathbf{e}} = 2(2GX_{0,n})^2\Delta\mathbf{e}. \end{cases} \tag{A.7}$$

Indeed, the following relations hold

$$\frac{\partial\Delta\widehat{\boldsymbol{\Psi}}}{\partial\mathbf{e}} = \frac{\partial\Delta\overline{\boldsymbol{\Psi}}_0}{\partial\mathbf{e}} + (1-\alpha)\frac{\partial\Delta\overline{\boldsymbol{\Psi}}_1}{\partial\mathbf{e}} - \Delta\overline{\boldsymbol{\Psi}}_1\otimes\boldsymbol{\upsilon}, \tag{A.8}$$

$$\frac{\partial\Delta\overline{\boldsymbol{\Psi}}_0}{\partial\mathbf{e}} = \mathbb{I} + \frac{\tilde{q}}{X_{0,n}}(\boldsymbol{\alpha}_n\otimes\Delta\mathbf{e}) : \frac{\partial\mathbf{X}_n^{s,\mathrm{e}}}{\partial\mathbf{e}} + \tilde{q}\boldsymbol{\alpha}_n\otimes\mathbf{n}_{\mathrm{e}} \tag{A.9}$$

$$+ \frac{H_{\mathrm{nl}}}{H_{\mathrm{iso}}}(\mathbf{n}_{\mathrm{e}} : \Delta\mathbf{e})\boldsymbol{\alpha}_n\otimes\frac{\partial\bar{q}}{\partial\mathbf{e}}, \tag{A.10}$$

$$\frac{\partial\Delta\overline{\boldsymbol{\Psi}}_1}{\partial\mathbf{e}} = \frac{1}{2}\frac{H_{\mathrm{nl}}}{2G}\left(\frac{\partial\mathbf{D}_{\boldsymbol{\alpha}}}{\partial\mathbf{e}}D_\gamma + \mathbf{D}_{\boldsymbol{\alpha}}\otimes\frac{\partial D_\gamma}{\partial\mathbf{e}} + \boldsymbol{\alpha}_n\otimes\frac{\partial D'_\gamma}{\partial\mathbf{e}}\right), \tag{A.11}$$

where

$$\tilde{q} = \frac{H_{\mathrm{nl}}}{H_{\mathrm{iso}}}\bar{q} = \frac{H_{\mathrm{nl}}}{2G_1 - H_{\mathrm{nl}}(\mathbf{n}_{\mathrm{e}} : \boldsymbol{\alpha})}, \tag{A.12}$$

$$\frac{\partial\bar{q}}{\partial\mathbf{e}} = \frac{H_{\mathrm{iso}}H_{\mathrm{nl}}}{(2G_1 - H_{\mathrm{nl}}(\mathbf{n}_{\mathrm{e}} : \boldsymbol{\alpha}_n))^2}X_{0,n}^{-1}\left(\frac{\partial\mathbf{X}_n^{s,\mathrm{e}}}{\partial\mathbf{e}}\right)\boldsymbol{\alpha}_n, \tag{A.13}$$

$$\frac{\partial\mathbf{D}_{\boldsymbol{\alpha}}}{\partial\mathbf{e}} = (H_{\mathrm{kin}}\mathbf{n}_{\mathrm{e}} - H_{\mathrm{nl}}\boldsymbol{\alpha}_n)\otimes\frac{\partial D_\gamma}{\partial\mathbf{e}} + H_{\mathrm{kin}}\frac{D_\gamma}{X_{0,n}}\frac{\partial\mathbf{X}_n^{s,\mathrm{e}}}{\partial\mathbf{e}}, \tag{A.14}$$

$$\frac{\partial D_\gamma}{\partial\mathbf{e}} = (\mathbf{n}_{\mathrm{e}} : \Delta\mathbf{e})\boldsymbol{\Phi} + \bar{q}\left(\mathbf{n}_{\mathrm{e}} + X_{0,n}^{-1}\frac{\mathbf{X}_n^{s,\mathrm{e}}}{\partial\mathbf{e}}\Delta\mathbf{e}\right), \tag{A.15}$$

$$\frac{\partial D'_\gamma}{\partial\mathbf{e}} = \mathbb{T}_4 + \mathbb{T}_5 + \mathbb{T}_6 \tag{A.16}$$

with $\mathbf{n}_{\mathrm{e}} = \mathbf{X}_n^{s,\mathrm{e}}/X_{0,n}$ the normalized stress at the end of the elastic part. The second-order tensors appearing in (A.15), (A.16) are given by the following expressions

$$\boldsymbol{\Phi} = X_{0,n}^{-1}\frac{2GH_{\mathrm{nl}}}{[2G_1 - H_{\mathrm{nl}}(\mathbf{n}_{\mathrm{e}} : \boldsymbol{\alpha}_n)]^2}\frac{\partial\mathbf{X}_n^{s,\mathrm{e}}}{\partial\mathbf{e}}\boldsymbol{\alpha}_n, \tag{A.17}$$

$$\mathbb{T}_4 = (\mathbf{n}_{\mathrm{e}} : \Delta\mathbf{e})\boldsymbol{\Phi} + \bar{q}\left(\mathbf{D}_{\mathbf{n}} + \frac{\partial\mathbf{D}_{\mathbf{n}}}{\partial\mathbf{e}}\Delta\mathbf{e}\right), \tag{A.18}$$

$$\mathbb{T}_5 = H_{\mathrm{nl}}[(\mathbf{D}_{\mathbf{n}} : \boldsymbol{\alpha}) + (\mathbf{n}_{\mathrm{e}} : \mathbf{D}_{\boldsymbol{\alpha}})]\left[\frac{2(\mathbf{n}_{\mathrm{e}} : \Delta\mathbf{e})}{2G_1 - H_{\mathrm{nl}}(\mathbf{n}_{\mathrm{e}} : \boldsymbol{\alpha}_n)}\boldsymbol{\Phi} + \frac{2G}{[2G_1 - H_{\mathrm{nl}}(\mathbf{n}_{\mathrm{e}} : \boldsymbol{\alpha}_n)]^2}\left(\mathbf{n}_{\mathrm{e}} + X_{0,n}^{-1}\frac{\partial\mathbf{X}_n^{s,\mathrm{e}}}{\partial\mathbf{e}}\Delta\mathbf{e}\right)\right], \tag{A.19}$$

$$\mathbb{T}_6 = \frac{2GH_{\mathrm{nl}}}{(2G_1 - H_{\mathrm{nl}}(\mathbf{n}_{\mathrm{e}} : \boldsymbol{\alpha}_n))^2}(\mathbf{n}_{\mathrm{e}} : \Delta\mathbf{e})\left[\frac{\partial\mathbf{D}_{\mathbf{n}}}{\partial\Delta\mathbf{e}}\boldsymbol{\alpha}_n + X_{0,n}^{-1}\frac{\partial\mathbf{X}_n^{s,\mathrm{e}}}{\partial\Delta\mathbf{e}}\mathbf{D}_{\boldsymbol{\alpha}} + \frac{\partial\mathbf{D}_{\boldsymbol{\alpha}}}{\partial\Delta\mathbf{e}}\mathbf{n}_{\mathrm{e}}\right] \tag{A.20}$$

with

$$\frac{\partial \mathbf{D}_{\mathbf{n}}}{\partial \Delta \mathbf{e}} = \frac{2G}{\sigma_{y,n}}\mathbb{I} - \frac{2G_1}{\sigma_{y,0}}\left[D_\gamma X_{0,n}^{-1}\frac{\partial \mathbf{X}_n^{s,e}}{\partial \Delta \mathbf{e}} + \mathbf{n}_e \otimes \frac{\partial D_\gamma}{\partial \Delta \mathbf{e}}\right] \tag{A.21}$$

$$+ \frac{H_{nl}}{\sigma_{y,n}}\boldsymbol{\alpha}_n \otimes \frac{\partial D_\gamma}{\partial \Delta \mathbf{e}}. \tag{A.22}$$

Let moreover

$$\frac{\partial \bar{\sigma}_y}{\partial \mathbf{e}} = \sigma_{y,n}\left(\frac{\log(1+c) - c/(1+c)}{2\log 1 + c}\right)\frac{\partial c}{\partial \mathbf{e}}, \tag{A.23}$$

where

$$\frac{\partial c}{\partial \mathbf{e}} = \frac{2G\bar{q}}{\sigma_{y,n}}\left[-(\mathbf{n}_e : \Delta \mathbf{e})\upsilon + \frac{(1-\alpha)}{X_{0,n}}\frac{\partial \mathbf{X}_n^{s,e}}{\partial \mathbf{e}}\Delta \mathbf{e}\right.$$

$$\left. +(1-\alpha)\mathbf{n}_e + \frac{1-\alpha}{\bar{q}}(\mathbf{n}_e : \Delta \mathbf{e})\frac{\partial \bar{q}}{\partial \mathbf{e}}\right], \tag{A.24}$$

$$\frac{\partial \mathbf{X}_n^{s,e}}{\partial \mathbf{e}} = \alpha\frac{2G}{\sigma_{y,n}}\mathbb{I} + \frac{2G}{\sigma_{y,n}}X_{0,n}(\Delta \mathbf{e} \otimes \upsilon). \tag{A.25}$$

Let in addition

$$\frac{\partial \|\Delta \widehat{\boldsymbol{\Psi}}\|}{\partial \mathbf{e}} = \frac{\partial \Delta \widehat{\boldsymbol{\Psi}}}{\partial \mathbf{e}}\frac{\Delta \widehat{\boldsymbol{\Psi}}}{\|\Delta \widehat{\boldsymbol{\Psi}}\|}, \tag{A.26}$$

$$\frac{\partial}{\partial \mathbf{e}}\left(\frac{\Delta \widehat{\boldsymbol{\Psi}}}{\|\Delta \widehat{\boldsymbol{\Psi}}\|}\right) = \|\Delta \widehat{\boldsymbol{\Psi}}\|^{-2}\left(\|\Delta \widehat{\boldsymbol{\Psi}}\|\frac{\partial \Delta \widehat{\boldsymbol{\Psi}}}{\partial \mathbf{e}} - \Delta \widehat{\boldsymbol{\Psi}} \otimes \frac{\partial \|\Delta \widehat{\boldsymbol{\Psi}}\|}{\partial \mathbf{e}}\right), \tag{A.27}$$

$$\frac{\partial a}{\partial \mathbf{e}} = b\frac{2G}{\bar{\sigma}_y}\left[-\|\Delta \widehat{\boldsymbol{\Psi}}\|\upsilon - (1-\alpha)\frac{\|\Delta \widehat{\boldsymbol{\Psi}}\|}{\bar{\sigma}_y}\frac{\partial \bar{\sigma}_y}{\partial \mathbf{e}} + (1-\alpha)\frac{\partial \|\Delta \widehat{\boldsymbol{\Psi}}\|}{\partial \mathbf{e}}\right], \tag{A.28}$$

$$\frac{\partial b}{\partial \mathbf{e}} = a\frac{2G}{\bar{\sigma}_y}\left[-\|\Delta \widehat{\boldsymbol{\Psi}}\|\upsilon - (1-\alpha)\frac{\|\Delta \widehat{\boldsymbol{\Psi}}\|}{\bar{\sigma}_y}\frac{\partial \bar{\sigma}_y}{\partial \mathbf{e}} + (1-\alpha)\frac{\partial \|\Delta \widehat{\boldsymbol{\Psi}}\|}{\partial \mathbf{e}}\right]. \tag{A.29}$$

The fourth-order tensors defined in (A.6) are thus:

$$\mathbb{T}_1 = \frac{\partial \mathbf{X}_n^{s,e}}{\partial \mathbf{e}} + \alpha\frac{2G}{\sigma_{y,n}}X_{0,n}\frac{a-1}{\|\Delta \widehat{\boldsymbol{\Psi}}\|^2}\Delta \widehat{\boldsymbol{\Psi}} \otimes \Delta \widehat{\boldsymbol{\Psi}}$$

$$+ \alpha\frac{2G}{\sigma_{y,n}}X_{0,n}\frac{a-1}{\|\Delta \widehat{\boldsymbol{\Psi}}\|^2}(\Delta \widehat{\boldsymbol{\Psi}} : \Delta \mathbf{e})\Delta \widehat{\boldsymbol{\Psi}} \otimes \upsilon, \tag{A.30}$$

$$\mathbb{T}_2 = \frac{(\Delta \widehat{\boldsymbol{\Psi}} : \mathbf{X}_n^{s,e})}{\|\Delta \widehat{\boldsymbol{\Psi}}\|^2}\Delta \widehat{\boldsymbol{\Psi}} \otimes \frac{\partial a}{\partial \mathbf{e}} + \frac{X_{0,n}}{\|\Delta \widehat{\boldsymbol{\Psi}}\|}\Delta \widehat{\boldsymbol{\Psi}} \otimes \frac{\partial b}{\partial \mathbf{e}}, \tag{A.31}$$

$$\mathbb{T}_3 = (a-1)\left(\frac{\Delta \widehat{\boldsymbol{\Psi}}}{\|\Delta \widehat{\boldsymbol{\Psi}}\|} : \mathbf{X}_n^{s,e}\right)\frac{\partial}{\partial \mathbf{e}}\left(\frac{\Delta \widehat{\boldsymbol{\Psi}}}{\|\Delta \widehat{\boldsymbol{\Psi}}\|}\right)$$

$$+ (a-1)\frac{\Delta \widehat{\boldsymbol{\Psi}}}{\|\Delta \widehat{\boldsymbol{\Psi}}\|} \otimes \left[\frac{\partial}{\partial \mathbf{e}}\left(\frac{\Delta \widehat{\boldsymbol{\Psi}}}{\|\Delta \widehat{\boldsymbol{\Psi}}\|}\right)\mathbf{X}_n^{s,e}\right]$$

$$+ bX_{0,n}\frac{\partial}{\partial \mathbf{e}}\left(\frac{\Delta \widehat{\boldsymbol{\Psi}}}{\|\Delta \widehat{\boldsymbol{\Psi}}\|}\right). \tag{A.32}$$

The scalar function X_0, following the algorithm of Section 4.1, is updated as

$$X_0 = b\frac{(\Delta \widehat{\boldsymbol{\Psi}} : \mathbf{X}_n^{s,e})}{\|\Delta \widehat{\boldsymbol{\Psi}}\|} + aX_{0,n}. \tag{A.33}$$

Therefore, a direct derivation gives

$$\frac{\partial X_0}{\partial \mathbf{e}} = \frac{(\Delta \widehat{\boldsymbol{\Psi}} : \mathbf{X}_n^{s,e})}{\|\Delta \widehat{\boldsymbol{\Psi}}\|}\frac{\partial b}{\partial \mathbf{e}} + \frac{b}{\|\Delta \widehat{\boldsymbol{\Psi}}\|}\frac{\partial \mathbf{X}_n^{s,e}}{\partial \mathbf{e}}\Delta \widehat{\boldsymbol{\Psi}}$$

$$+ b\left(\frac{\partial}{\partial \mathbf{e}}\frac{\Delta \widehat{\boldsymbol{\Psi}}}{\|\Delta \widehat{\boldsymbol{\Psi}}\|}\right)\mathbf{X}_n^{s,e} + X_{0,n}\frac{\partial a}{\partial \mathbf{e}}, \tag{A.34}$$

which is readily calculated in view of the previous derivations in this appendix.

Finally, with respect to the derivative of the backstress α for an elastoplastic step, it holds

$$\frac{\partial \boldsymbol{\alpha}}{\partial \mathbf{e}} = \left(H_{kin}\frac{\partial \Delta \mathbf{e}^p}{\partial \mathbf{e}} - \frac{1}{2}H_{nl}\boldsymbol{\alpha}_n \otimes \frac{\partial \Delta \gamma}{\partial \mathbf{e}}\right)\left(1 + \frac{1}{2}H_{nl}\Delta \gamma\right)^{-1}$$

$$- \frac{H_{nl}}{2}\left(1 + \frac{1}{2}H_{nl}\Delta \gamma\right)^{-2}\left[H_{kin}\Delta \mathbf{e}^p + \left(1 - \frac{1}{2}H_{nl}\Delta \gamma\right)\boldsymbol{\alpha}_n\right]$$

$$\otimes \frac{\partial \Delta \gamma}{\partial \mathbf{e}}, \tag{A.35}$$

where

$$\Delta \mathbf{e}^p = \frac{1}{2}\Delta \gamma\left(\frac{\mathbf{X}^s}{X_0} + \frac{\mathbf{X}_n^s}{X_{0,n}}\right), \tag{A.36}$$

$$\frac{\partial \Delta \gamma}{\partial \mathbf{e}} = \begin{cases} q\dfrac{\sigma_{y,0}}{H_{iso}}X_0^{q-1}\dfrac{\partial X_0}{\partial \mathbf{e}} & \text{if } H_{iso} = 0, \\ \dfrac{\sigma_{y,0}}{2G_1}\dfrac{X_{0,n}}{X_0}\dfrac{\partial X_0}{\partial \mathbf{e}} & \text{if } H_{iso} \neq 0, \end{cases} \tag{A.37}$$

$$\frac{\partial \Delta \mathbf{e}^p}{\partial \mathbf{e}} = \frac{1}{2}\Delta \gamma\frac{\partial}{\partial \mathbf{e}}\left(\frac{\mathbf{X}^s}{X_0}\right) + \frac{1}{2}\left[\left(\frac{\mathbf{X}^s}{X_0} + \frac{\mathbf{X}_n^s}{X_{0,n}}\right) \otimes \frac{\partial \Delta \gamma}{\partial \mathbf{e}}\right], \tag{A.38}$$

$$\frac{\partial}{\partial \mathbf{e}}\left(\frac{\mathbf{X}^s}{X_0}\right) = \frac{1}{X_0}\frac{\partial \mathbf{X}^s}{\partial \mathbf{e}} - \frac{1}{X_0^2}\left(\mathbf{X}^s \otimes \frac{\partial X_0}{\partial \mathbf{e}}\right). \tag{A.39}$$

References

[1] E. Artioli, F. Auricchio, L. Beirao da Veiga, Integration schemes for von-Mises plasticity models based on exponential maps: numerical investigations and theoretical considerations, Int. J. Numer. Methods Engrg. 64 (2005) 1133–1165.

[2] E. Artioli, F. Auricchio, L. Beirao da Veiga, A novel "optimal" exponential-based integration algorithm for von-Mises plasticity with linear hardening: theoretical analysis on yield consistency, accuracy, convergence and numerical investigations, Int. J. Numer. Methods Engrg. 67 (4) (2006) 449–498.

[3] P.J. Armstrong, C.O. Frederick, A mathematical representation of the multi-axial Baushinger effect, Technical Report C.E.G.B. Report RD/B/N731, Berkeley Nuclear Laboratories, R&D Department, 1966.

[4] F. Auricchio, R.L. Taylor, Two material models for cyclic plasticity: nonlinear kinematic hardening and generalized plasticity, Int. J. Plasticity 11 (1995) 65–98.

[5] F. Auricchio, Ce-driver, Technical report, Dipartimento di Meccanica Strutturale – University of Pavia, Manual prepared for the European School of Advanced Studies of Seismic Risk Reduction, 2001.

[6] S. Hartman, P. Haupt, Stress computation and consistent tangent operator using non-linear kinematic hardening models, Int. J. Numer. Methods Engrg. 36 (1993) 3801–3814.

[7] Hong-Ki Hong, Chien-Shan Liu, Internal symmetry in bilinear elastoplasticity, Int. J. Non-Linear Mech. 34 (1999) 279–288.
[8] Hong-Ki Hong, Chien-Shan Liu, Lorentz group on Minkowski spacetime for construction of the two basic principles of plasticity, Int. J. Non-Linear Mech. 36 (2001) 679–686.
[9] Hong-Ki Hong, Chien-Shan Liu, Some physical models with Minkowski spacetime structure and Lorentz group symmetry, Int. J. Non-Linear Mech. 36 (2001) 1075–1084.
[10] IMSL – Fortran Subroutines for Mathematical Applications. Math/Library. Vols. 1 and 2, Visual Numerics, 1997.
[11] A. Iserles, A First Course in the Numerical Analysis of Differential Equations, Cambridge University Press, 1997.
[12] R.D. Krieg, D.B. Krieg, Accuracies of numerical solution methods for the elastic–perfectly plastic model, J. Pressure Vessel Technol., Trans. ASME 99 (1977) 510–515.
[13] J.D. Lambert, Numerical Methods for Ordinary Differential Systems: The Initial Value Problem, John Wiley & Sons, Chichester, 1973.
[14] Chien-Shan Liu, Chi-Fu Li, Geometrical numerical algorithms for a plasticity model with Armstrong Frederick kinematic hardening rule under strain and stress controls, Int. J. Numer. Methods Engrg. 63 (2005) 1396–1423.
[15] M. Ortiz, E.P. Popov, Accuracy and stability of integration algorithms for elastoplastic constitutive relations, Int. J. Numer. Methods Engrg. 21 (1985) 1561–1576.
[16] M. Ortiz, J.C. Simo, An analysis of a new class of integration algorithms for elastoplastic constitutive relations, Int. J. Numer. Methods Engrg. 23 (1986) 353–366.
[17] J.C. Simo, S. Govindjee, Non-linear B-stability and symmetry preserving return mapping algorithms for plasticity and viscoplasticity, Int. J. Numer. Methods Engrg. 31 (1991) 151.
[18] J.C. Simo, T.J.R. Hughes, Computational Inelasticity, Springer-Verlag, 1998.
[19] J.C. Simo, Topics on the numerical analysis and simulation of plasticity, in: P.G. Ciarlet, J.L. Lions (Eds.), Handbook of Numerical Analysis, vol. III, Elsevier Science Publisher B.V., 1999.
[20] J.C. Simo, R.L. Taylor, Consistent tangent operators for rate-independent elasto-plasticity, Comput. Methods Appl. Mech. Engrg. 48 (1985) 101.
[21] J.C. Simo, R.L. Taylor, A return mapping algorithm for plane stress elastoplasticity, Int. J. Numer. Methods Engrg. 22 (1986) 649–670.
[22] R.L. Taylor, A finite element analysis program, Version 7.5 user manual, Technical report, University of California at Berkeley, 2003, http://www.ce.berkeley.edu/rlt.
[23] Ch. Tsakmakis, A. Willuweit, A comparative study of kinematic hardening rules at finite deformations, Int. J. Non-Linear Mech. 39 (2004) 539–554.
[24] C.H. Wang, W. Hu, J.P.G. Sawyer, Explicit numerical integration algorithm for a class of non-linear kinematic hardening model, Comput. Mech. 26 (2000) 140–147.
[25] O.C. Zienkiewicz, R.L. Taylor, The Finite Element Method, fifth ed., vol. II, McGraw Hill, New York, 2002.